An Extended CNMF-Based Hyperspectral and Multispectral Image Fusion Approach for Addressing Spectral Variability

Fatima Zohra Benhalouche[a,b,*], Moussa Sofiane Karoui[a,b], Yannick Deville[b]

[a]*Agence Spatiale Algérienne, Centre des Techniques Spatiales, 31200 Arzew, Algeria*

[b]*Institut de Recherche en Astrophysique et Planétologie (IRAP), Université de Toulouse, CNRS, OMP, CNES, 31400 Toulouse, France*

* Correspondence: Fatima.Benhalouche@irap.omp.eu

An Extended CNMF-Based Hyperspectral and Multispectral Image Fusion Approach for Addressing Spectral Variability

Abstract

The hyperspectral and multispectral image fusion process, commonly known as the multisharpening process (also known as the hypersharpening process), results in the creation of unobservable high spectral and spatial resolution hyperspectral remote sensing data, by combining (or fusing) a hyperspectral image, characterised by a high spectral resolution, with, especially, a high spatial resolution multispectral one. There are several approaches in the literature performing such a process, in particular those based on the spectral unmixing concept. The latter fusion methods aim to extract pure-material spectra from the high spectral resolution hyperspectral image and combine them with their corresponding proportions extracted from the high spatial resolution multispectral image. However, most of these methods, which mainly consider the standard linear mixing model, do not address the spectral variability phenomenon, precisely due to the considered data mixing model, which does not handle variations in illumination and atmospheric conditions or material composition inducing spectral variability. Neglecting such a phenomenon may lead to errors in the fusion process, thus decreasing the spatial and spectral qualities of sharpened products. In this paper, a new hyperspectral and multispectral data fusion method, based on the linear spectral unmixing concept that deals with spectral variability, is proposed. This approach, based on a multiplicative Nonnegative Matrix Factorization (NMF) technique, substantially extends the multiplicative Coupled NMF (CNMF) algorithm by considering a linear data mixing model that addresses the considered phenomenon. Indeed, the introduced approach minimises new cost functions involving matrices with specific structures in order to deal with the spectral variability phenomenon. The proposed method is applied to synthetic and real data, and its effectiveness is evaluated with established performance criteria. Experimental results show that the designed algorithm globally yields sharpened hyperspectral data with fine spectral and spatial fidelities. Also, these results demonstrate that the proposed technique globally outperforms the tested literature approaches.

Keywords: Hyper/multispectral imaging, data fusion, hyperspectral and multispectral image fusion, hyper/multisharpening, spectral/intra-class variability, linear spectral unmixing, nonnegative matrix factorization.

1. Introduction

The hyperspectral and multispectral image fusion technique, widely known as the multisharpening technique, is a well-known process in the field of remote sensing image processing (Vivone 2023). This process is often used to improve the spatial resolution of observable hyperspectral data, which are generally characterised by their high spectral resolution, whereas their spatial resolution is low. Also known as hypersharpening, this process allows fusing such data with observable panchromatic or, in particular, multispectral images, of the same scene, with a higher spatial resolution (Loncan et al. 2015; Yokoya, Grohnfeldt, and Chanussot 2017). The resulting unobservable fused hyperspectral data allow, in particular, accurate classification of an observed area at a finer spatial resolution.

Several categories of sharpening methods have been proposed in the literature. The first category includes methods known as pansharpening techniques (Loncan et al. 2015; Chen 2012; Vivone et al. 2015). They were first proposed to improve the spatial resolution of multispectral data by using the spatial information contained in a high spatial resolution panchromatic image (Loncan et al. 2015). With the advent of hyperspectral remote sensing sensors, these methods have evolved towards hyperspectral and panchromatic data fusion.

Recently a second category of sharpening methods has emerged, including fusion methods that consider the multisharpening process. This process aims to improve the spatial resolution of observed hyperspectral images, by merging their spectral information with spatial information obtained, especially, from observed high spatial resolution multispectral images, thus generating unobservable hyperspectral data with high spectral and spatial resolutions (Yokoya, Grohnfeldt, and Chanussot 2017; Eismann and Hardie 2005; Selva et al. 2015; Huang 2014; Chen et al. 2014; Simoes et al. 2015; Lu et al. 2019; Karoui et al. 2017; Benhalouche et al. 2017; Dian et al. 2018; Tsagkatakis et al. 2019; Dian et al. 2021; Lu et al. 2022; Hu et al. 2022;

Khader, Xiao, and Yang 2022). Indeed, numerous methods have been proposed to apply the multisharpening process to hyperspectral data. Some of them are based on the Linear Spectral Unmixing (LSU) concept (Bioucas-Dias et al. 2012) and use Nonnegative Matrix Factorization (NMF) (Cichocki et al. 2009). Standard LSU techniques consist of linearly and blindly unmixing remote sensing images (Deville 2016), in order to estimate a collection of pure-material (also called endmember) spectra and their corresponding abundance fractions (which correspond to their occupied surface proportions) (Bioucas-Dias et al. 2012). These classical LSU approaches are based on: 1) the Linear Mixture Model (LMM), in which each observed pixel spectrum is considered as a linear mixture of contributions from several endmember spectra that are present in the observed scene and 2) the assumption that each endmember is represented, in the whole image, only by a single spectrum (Bioucas-Dias et al. 2012). However, the latter assumption is no longer valid in many configurations. Indeed, in real-world scenarios, mixing phenomena tend to be considerably more complex. This is especially true when the observed scene includes significant variations in relief and/or irradiance heterogeneity (for example, when sunlight successively reflects off several surfaces before reaching the sensor). Such conditions are common in urban environments, where the standard linear mixing model no longer holds, and the mixing model inevitably becomes non-linear (José M. P. Nascimento and Bioucas-Dias 2009; Halimi et al. 2011; Heylen, Parente, and Gader 2014; Meganem et al. 2014; Heylen and Scheunders 2016; Luo et al. 2016; Yang, Wang, and Wu 2018; Gu, Yang, and Wang 2022). Furthermore, another phenomenon, frequently observed in real-world scenarios, is spectral/intra-class variability (Zare and Ho 2014; Revel et al. 2018; Benhalouche, Karoui, and Deville 2019). This phenomenon is particularly pronounced when the observed scene exhibits fluctuations due to variations in lighting, atmospheric conditions, or material composition (Borsoi et al. 2021). Consequently, the concept of endmembers should be replaced by the notion of endmember classes. Failure to take this phenomenon of spectral/intra-class variability into account may lead to propagating errors throughout the analysis of data under consideration (Borsoi et al. 2021).

Therefore, it has become essential to address the spectral variability phenomenon in the spectral unmixing process. This has led to the development of some linear data mixing models and their associated unmixing algorithms, which integrate that phenomenon and model it in various forms (Borsoi et al. 2021). Among these advanced linear models, the following may be mentioned. The Extended LMM (ELMM), proposed in (Drumetz et al. 2016), scales each endmember spectrum, pixel by pixel, by a single constant for all considered spectral bands. The Perturbed LMM (PLMM), reported in (Thouvenin, Dobigeon, and Tourneret 2016), adds a perturbation to the reference endmember spectra to represent spectral variability. The Generalized LMM (GLMM), detailed in (Imbiriba, Borsoi, and Moreira Bermudez 2018), uses a matrix of scaling factors of the same dimension as the endmember spectra matrix to represent spectral variability. Considering that there is a spectral variability other than scale factors, which models variations not only spectrally, across different wavelengths, but also spatially, i.e. in each pixel of the processed image, the Augmented LMM (ALMM), and its modified version (mALMM), were proposed in (Hong et al. 2019; Karoui, Benhalouche, and Deville 2022). These models consider more spectral variabilities by adding, to scaling factors, other types of spectral variability. Other models, proposed in (Benhalouche, Karoui, and Deville 2019; Brezini et al. 2021), deal with spectral variability by also considering individual variability coefficients for each pixel and for each spectral band of a pure material.

In recent years, considering complex mixing phenomena in real-world scenarios has become a major issue in the multisharpening process. Indeed, the limitations of linear mixing models have led to the investigation of more advanced multisharpening approaches, first incorporating non-linear mixing models. Integrating these non-linear models has improved the representation of complex interactions between materials in an observed scene, by considering multiple reflections and non-homogeneous scattering due to the environment (Benhalouche et al. 2017; Priya, and Rajkumar 2022; Z. Wang et al. 2022; Vivone 2023). This methodological advance has contributed to more accurate analyses and more refined multisharpening results.

More recently, some unmixing-based hyperspectral and multispectral data fusion methods were developed, involving complex mixing models, to address spectral variability issues (Borsoi, Imbiriba, and Bermudez 2020; W. Liu et al. 2020; Karoui et al. 2021; Benhalouche et al. 2022; Brezini et al. 2022; Camacho, Vargas, and Arguello 2022). In (Borsoi, Imbiriba, and Bermudez 2020), the spectral variability phenomenon has been addressed in the fusion problem only in the context of seasonal spectral variability (i.e., the spectral variations of materials, present in an imaged scene, are due to different acquisitions and seasonal conditions). This approach mainly deals with seasonal changes using a subspace/unmixing-based formulation, and by considering a unique set of endmember spectra for each image and a parametric model to represent variations of hyperspectral material spectra over time, which may differ considerably from multispectral ones. In (Brezini et al. 2022), the authors proposed an NMF-unmixing-based multisharpening approach, based on an extended version of the NMF-unmixing technique, called Inertia-Constrained Pixel-by-Pixel Nonnegative Matrix Factorization (IP-NMF) (Revel et al. 2018), which takes into account the phenomenon of spectral variability. The used model considers a different spectrum for each endmember in each pixel of considered hyperspectral and multispectral data (Brezini et al. 2022). In (Camacho, Vargas, and Arguello 2022), the proposed unmixing-based fusion method deals with spectral variability by using ALMM (Hong et al. 2019), which simultaneously accounts for scaling factors and other types of spectral variability. This fusion approach uses an alternating optimization strategy combined with the alternating direction method of multipliers (Boyd 2010) to minimize the fusion problem cost function.

Furthermore, it is important to emphasise that, in recent years, new Deep Learning (DL)-based techniques emerged in the field of remote sensing data fusion (Vivone 2023; Vivone et al. 2025). These approaches take advantage of machine learning through deep neural network architectures, including convolutional neural networks, autoencoders, attention mechanisms, and transformers. Initially developed for pansharpening (Vivone et al. 2021), these methods have been extended to include the fusion of hyperspectral images with multispectral data (Palsson, Sveinsson, and Ulfarsson 2017; Dian et al. 2018; Vali, Comai, and Matteucci 2020; Li et al. 2022; Khader, Xiao, and Yang 2022). DL-based fusion techniques include: i) supervised approaches, which require large labelled training datasets and may not generalise well to datasets not included in the training process, and ii) unsupervised ones that learn directly from input images (Vivone et al. 2025). It is also worth noting that there exist some advanced DL-based fusion methods that consider more complex data mixing models, with spectral variability taken into account (Wang et al. 2023; Zheng et al. 2024; Han et al. 2025).

In the present work, a new NMF-unmixing-based hyperspectral and multispectral data fusion algorithm is proposed. It is inspired from the literature method (Yokoya, Yairi, and Iwasaki 2012), which has demonstrated its effectiveness in the field of hyperspectral and multispectral data fusion. The latter method is here substantially extended so as to consider the spectral variability phenomenon, using the multiplicative data mixing model introduced in (Benhalouche, Karoui, and Deville 2019). Thus, the proposed algorithm significantly extends the multiplicative Coupled NMF (CNMF) technique (Yokoya, Yairi, and Iwasaki 2012) for addressing spectral variability. It consists of alternately unmixing the considered observable data, by exploiting a spatial degradation model between the considered observable hyperspectral and multispectral used data, and it takes into account the specific structure of involved matrices that address the spectral variability phenomenon only for hyperspectral data.

This paper is organized in the following manner. The motivations of this work and all its contributions are reported in Section 2. The considered data mixing model, accounting for spectral variability, is introduced in Section 3. Then, the steps involved in the designed fusion approach are described in Section 4. The used synthetic and real data are presented in Section 5. In Section 6, the results obtained with the conducted experiments are presented. These achieved results are also compared to those obtained by approaches from the literature. Also, in Section 6, all obtained results, based on tested data, are discussed. Finally, Section 7 concludes this paper.

2. Motivations and Contributions

As mentioned above, the approach introduced in this work substantially extends the CNMF method proposed in (Yokoya, Yairi, and Iwasaki 2012). The main motivation for using the CNMF-based unmixing method as the basis for the designed fusion approach is founded on several factors. First, the CNMF method is widely recognized in the literature for its high performance and robustness, which have been demonstrated through numerous studies (Benhalouche et al. 2017; T. Wang, Zhang, and Lin 2017; Lin et al. 2018; Priya, and Rajkumar 2021). Its efficiency makes it a particularly good choice for hyperspectral and multispectral data fusion, especially in applications where preserving spectral and spatial characteristics is essential. Another major advantage of this method is its reproducibility. Indeed, its well-established algorithmic framework allows it to be easily implemented, making its extension accessible. Based on these main advantages, a substantial extension of the CNMF method is proposed in this investigation to incorporate spectral variability, a crucial aspect in many data fusion scenarios. This enhancement aims to further optimize the performance of the fusion process, taking into account spectral variations that can influence fusion quality.

Moreover, from an algorithmic point of view, the proposed approach combines and also extends the approaches proposed in (Benhalouche, Karoui, and Deville 2019; Benhalouche et al. 2022). Indeed, in (Benhalouche et al. 2022), the focus was on developing an approach that extends the CNMF technique, which aims to iteratively unmix the observed data, by exploiting a spectral/spatial degradation model between the two processed images. In addition, it takes into account the specific structure of the matrices involved, as modelled in (Revel et al. 2018), to address spectral variability. Moreover, the work reported here extends the approach described in (Benhalouche et al. 2022), adopting the data mixing model introduced in (Benhalouche, Karoui, and Deville 2019), where spectral variability is multiplicatively modelled, so that each endmember spectrum is associated with a non-negative spectral variability coefficient. This coefficient adjusts the endmember spectrum to reflect its specificity in each hyperspectral image pixel, enabling finer modelling of spectral variations within the manipulated hyperspectral image.

A further original feature of this work is the reformulation of the model presented in (Benhalouche, Karoui, and Deville 2019). Such a reformulation offers a significant advantage. Indeed, it allows one to extract a unique set of endmember spectra, considered as reference spectra, representative of the averages of the spectra present within each pixel of the manipulated hyperspectral image. Then, this set of reference spectra will serve as input data for the designed coupled unmixing approach for updating multispectral spectra. Thus, this data model reformulation enables handling lower-dimensional matrix variables, which considerably reduces computation times.

To sum up, and regardless of experiments that may be conducted, the main advantages of the proposed fusion approach are: 1) It is an unmixing-based one, thus with spectral and spatial features that are potentially richer and more relevant than those involved in non-unmixing-based fusion methods. 2) It deals with spectral variability, thus, it is expected to perform better than methods that do not take spectral variability into account. 3) It is an unsupervised physically interpretable model-based method, therefore, it is quite reasonable to expect it to perform faster and better than unsupervised data-driven methods, such as unsupervised DL-based techniques. Supervised DL methods, or supervised approaches based on neural networks in general, may perform better, but this remains very highly dependent on the learning carried out and the availability of the samples needed for it. 4) The proposed method uses a multiplicative mixing model, which covers a wider class of spectral variability than other models such as the ELMM and ALMM ones (Borsoi et al. 2021), due to its construction and the dimension of its involved variables. Indeed, ELMM uses only a single scale factor, applied uniformly to all wavelengths, per image pixel, while ALMM involves additional variables to represent other types of spectral variability in each pixel, but these variables are of dimensions lower than those used in the considered multiplicative model. 5) Unlike other unmixing-based fusion approaches dealing with spectral variability, the designed fusion method considers the used multiplicative mixing model only for hyperspectral data, which allows improving computational performances.

3. Considered data models

In this section, the different data mixing models, considered in the designed unmixing-based fusion approach, are introduced.

3.1. Standard linear mixing model

One of the considered data mixing models is the standard linear mixing model (LMM) (Bioucas-Dias et al. 2012), which assumes that each observed spectral vector is a linear combination of pure spectral signatures, referred to as endmembers, weighted by their proportions. Mathematically, an observed image $\mathbf{X} \in \mathbb{R}_{+}^{L\times \mathrm{P}}$ is, therefore, modelled in matrix form as follows

$$\mathbf{X} = \mathbf{E_{ref}}\, \mathbf{C_s}, \qquad (1)$$

where $\mathbf{X} = [\boldsymbol{x_1} \dots \boldsymbol{x_P}]$, a nonnegative matrix with a dimension of $L \times P$, contains the observed pixel spectra. Each row of this matrix represents one spectral band, and each column represents an observed pixel spectrum. L and P respectively correspond to the number of spectral bands and the number of pixels of the considered image. $\mathbf{E_{ref}} \in \mathbb{R}_+^{L\times M}$ is the nonnegative endmember matrix: each of its columns contains one endmember spectrum. M is the number of endmembers. $\mathbf{C_s} \in \mathbb{R}_+^{M\times P}$ corresponds to the nonnegative abundance fractions matrix, with index s standing for "standard" (Bioucas-Dias et al. 2012). Each row of this matrix contains all abundance fractions, in all pixels of the considered image, of one endmember.

3.2. Linear mixing model addressing spectral variability

In order to address the spectral variability phenomenon, a second data mixing model is considered. Indeed, as stated above, the designed NMF-unmixing-based multisharpening algorithm considers the data mixing model proposed in (Benhalouche, Karoui, and Deville 2019). This model involves matrices with a specific structure in order to deal with the spectral variability phenomenon. Thus, an observed image $\mathbf{X}$ is modelled in matrix form as follows

$$\mathbf{X} = (\mathbf{A} \odot \mathbf{E})\, \mathbf{C}, \tag{2}$$

where the operator $\odot$ denotes the matrix element-wise multiplication. The nonnegative matrix $\mathbf{A} \in \mathbb{R}_+^{L\times(PM)}$, where M refers to the number of classes of endmembers, contains all nonnegative spectral variability coefficients (Benhalouche, Karoui, and Deville 2019). This matrix is composed of P nonnegative sub-matrices $\mathbf{A_i} \in \mathbb{R}_+^{L\times M}$ $(i = 1 \ldots P)$: each of them contains nonnegative spectral variability coefficients associated with a given pixel i. Thus, this matrix can be written as

$$\mathbf{A} = [\mathbf{A_1}|\mathbf{A_2}| \quad \cdots \quad |\mathbf{A_P}], \tag{3}$$

$$\text{with } \mathbf{A_i} \in \mathbb{R}_{+}^{L\times M} \ \ (i = 1 \dots P).$$

Moreover, the nonnegative matrix $\mathbf{E} \in \mathbb{R}_{+}^{L\times(PM)}$ contains the nonnegative sub-matrix $\mathbf{E_{ref}}$, which corresponds to the M reference endmember spectra, replicated P times. Once again, each column of this sub-matrix contains one reference endmember spectrum. Consequently, this matrix has the following structure

$$\mathbf{E} = \underbrace{[\mathbf{E_{ref}}|\mathbf{E_{ref}}| \dots |\mathbf{E_{ref}}]}_{P}. \tag{4}$$

Besides, to preserve the specific structure of $\mathbf{E}$, it can be written as

$$\mathbf{E} = \mathbf{E_{ref}}\mathbf{K}, \tag{5}$$

where the nonnegative matrix $\mathbf{K} \in \mathbb{R}_{+}^{M\times(PM)}$contains the identity matrix, of dimension $M \times M$, replicated P times.

The nonnegative matrix $\mathbf{C} \in \mathbb{R}_{+}^{(PM)\times P}$ is a block-diagonal matrix that contains abundance fractions. This matrix is organized as follows (Revel et al. 2018)

$$\mathbf{C} = \begin{bmatrix} \boldsymbol{c}_{1,1} & \mathbf{0} & & \mathbf{0} \\ \vdots & \vdots & \cdots & \vdots \\ \boldsymbol{c}_{1,M} & \mathbf{0} & & \mathbf{0} \\ \mathbf{0} & \boldsymbol{c}_{2,1} & & \mathbf{0} \\ \vdots & \vdots & \ddots & \vdots \\ \mathbf{0} & \boldsymbol{c}_{2,M} & & \mathbf{0} \\ \mathbf{0} & \mathbf{0} & & \boldsymbol{c}_{p,1} \\ \vdots & \vdots & \cdots & \vdots \\ \mathbf{0} & \mathbf{0} & & \boldsymbol{c}_{p,M} \end{bmatrix}, \tag{6}$$

where $[\boldsymbol{c}_{i,1} \dots \boldsymbol{c}_{i,M}]^{T}$ is a column vector with M elements, which contains abundance fractions related to the i$^{\text{th}}$ observed pixel spectrum ($(.)^{T}$represents the vector/matrix transpose). Based on the above, the final second mixing model, which deals with the spectral variability phenomenon, is written as follows

$$\mathbf{X} = (\mathbf{A} \odot (\mathbf{E_{ref}} \mathbf{K}))\ \mathbf{C}. \tag{7}$$

3.3. Adopted mixing models

In the present investigations, two types of images are jointly considered. The first one is a high-spectral/low-spatial resolution hyperspectral image, denoted $\mathbf{X_h} \in \mathbb{R}_+^{L_h \times P_h}$, and the second considered image is a low-spectral/high-spatial resolution multispectral one, denoted $\mathbf{X_m} \in \mathbb{R}_+^{L_m \times P_m}$. L_h and P_h (respectively L_m and P_m) are, respectively, the numbers of spectral bands and pixels of the hyperspectral (respectively multispectral) image. These two images are supposed to be geometrically coregistered and radiometrically corrected.

In this work, it is assumed to be more relevant to address the spectral variability phenomenon only when considering hyperspectral data. Indeed, given the high spectral resolution of the remote sensing hyperspectral data, these data are more prone to allowing this phenomenon to be observed. Thus, a considered hyperspectral image is modelled as follows

$$\mathbf{X_h} = \left(\mathbf{A_h} \odot (\mathbf{E_{ref_h}} \mathbf{K_h})\right)\ \mathbf{C_h}, \tag{8}$$

where $\mathbf{C_h} \in \mathbb{R}_+^{(P_h M) \times P_h}$ contains low spatial resolution abundance fractions that are organized as described in (6), and the matrix $\mathbf{E_{ref_h}} \in \mathbb{R}_+^{L_h \times M}$ is the matrix composed of the M reference nonnegative hyperspectral endmember spectra. $\mathbf{A_h} \in \mathbb{R}_+^{L_h \times (P_h M)}$ contains all nonnegative hyperspectral coefficients of spectral variability. $\mathbf{K_h} \in \mathbb{R}_+^{M \times (P_h M)}$ contains the identity matrix, of dimension $\mathrm{M} \times \mathrm{M}$, replicated $\mathrm{P_h}$ times.

Given their low spectral resolution, multispectral data are modelled, without taking into account the phenomenon of spectral variability, through the standard linear mixing model (1):

$$\mathbf{X_m} = \mathbf{E_{ref_m}}\,\mathbf{C_{s_m}}, \tag{9}$$

where $\mathbf{C_{s_m}} \in \mathbb{R}_+^{M \times P_m}$ contains high spatial resolution abundance fractions, and the matrix $\mathbf{E_{ref_m}} \in \mathbb{R}_+^{L_m \times M}$ contains the M nonnegative multispectral endmember spectra.

Such a configuration, of the considered data mixing model (9), may reduce the computational time when manipulating very large matrices, as is the case for the multispectral abundance fractions matrix.

4. Proposed fusion method

4.1. Main processes involved in the proposed fusion algorithm

The designed fusion algorithm is inspired from a multiplicative NMF algorithm (Cichocki et al. 2009) and mainly consists in deriving (from the considered data): i) $\mathbf{\tilde{E}_{ref_h}}$ and $\mathbf{\widetilde{A}_h}$ that respectively estimate $\mathbf{E_{ref_h}}$ and $\mathbf{A_h}$, and ii) $\mathbf{\tilde{C}_{s_m}}$, which estimates $\mathbf{C_{s_m}}$, as detailed further in this paper.

To derive the above matrix estimates, the proposed fusion algorithm includes two LSU-unmixing processes and uses an NMF multiplicative algorithm, with the specific structure of the involved variables (Benhalouche, Karoui, and Deville 2019). The main building blocks, which are the essential processes of the proposed algorithm's overall functionality, take the following forms:

4.1.1. Process 1: hyperspectral image unmixing process

The first process consists in unmixing the hyperspectral image by optimising the following criterion

$$\mathrm{J}_1 = \frac{1}{2}\left\|\mathbf{X_h} - (\tilde{\mathbf{A}}_{\mathbf{h}} \odot (\tilde{\mathbf{E}}_{\mathbf{ref_h}}\mathbf{K_h}))\tilde{\mathbf{C}}_{\mathbf{h}}\right\|_{\mathrm{F}}^2 + \frac{\alpha}{2}\left\|\mathbf{1}^{\mathrm{L_h}\times(\mathrm{P_h M})} - \tilde{\mathbf{A}}_{\mathbf{h}}\right\|_{\mathrm{F}}^2, \qquad (10)$$

where $\|.\|_F$ denotes the Frobenius norm. $\mathbf{1}^{L_h \times P_h M}$ is a matrix of dimension $L_h \times (P_h M)$, where each element is equal to one. The last term of the cost function J_1 defined in (10) corresponds to a regularisation/penalisation term. Its purpose is to further constrain the estimated variability coefficients, in all observed pixels, in order to ensure that they remain close to the value 1. This limits the magnitude of the estimated spectral variability. The coefficient α is a positive balancing coefficient that controls the influence of the spectral variability regularisation/penalisation term. It should be noted that, in its basic version, the designed approach could proceed without the above additional term (by setting the coefficient α at 0), which corresponds to unconstrained spectral variability. This may be useful when the imaged scene contains significant spectral variability. On the contrary, when the imaged scene contains low or moderate spectral variability, the addition of the above additional term may be useful.

4.1.2. Process 2: multispectral image unmixing process

The second process optimises the following criterion in order to unmix the multispectral image

$$\mathrm{J}_2 = \frac{1}{2}\left\|\mathbf{X_m} - \tilde{\mathbf{E}}_{\mathbf{ref_m}}\tilde{\mathbf{C}}_{\mathbf{s_m}}\right\|_{\mathrm{F}}^2. \qquad (11)$$

4.1.3. Process 3: resizing matrices

This process is an essential step in harmonising the hyperspectral and multispectral matrix dimensions involved in the designed fusion approach. This requirement stems from the fact that hyperspectral matrix variables are modelled in order to include the spectral variability. In contrast, multispectral matrix variables, due to their low spectral resolution, are modelled without considering this phenomenon.

It should here be noted that $\tilde{\mathbf{C}}_{\mathbf{s_m}} \in \mathbb{R}_{+}^{M \times P_m}$ is not subsequently used in its original form: it is reorganised as a block-diagonal matrix that contains high-spatial resolution abundance fractions as described in (6) in order to obtain the matrix $\tilde{\mathbf{C}}'_{\mathbf{s_m}} \in \mathbb{R}_{+}^{(P_m M) \times P_m}$ that will be used in the fusion process described below (see Process 4). Similarly, the matrix $\left(\tilde{\mathbf{A}}_{\mathbf{h}} \odot (\tilde{\mathbf{E}}_{\mathbf{ref_h}} \mathbf{K_h})\right) \in \mathbb{R}_{+}^{L_h \times (P_h M)}$ is not subsequently used in its original form. Indeed, this matrix has a size that does not allow its direct manipulation in the fusion stage of the proposed sharpening approach. Thus, this matrix is used to create another one, denoted $\left(\tilde{\mathbf{A}}_{\mathbf{h}} \odot (\tilde{\mathbf{E}}_{\mathbf{ref_h}} \mathbf{K_h})\right)_{\mathbf{m}} \in \mathbb{R}_{+}^{L_h \times (P_m M)}$, by replicating the values of $\left(\tilde{\mathbf{A}}_{\mathbf{h}} \odot (\tilde{\mathbf{E}}_{\mathbf{ref_h}} \mathbf{K_h})\right)$ at the appropriate positions of $\left(\tilde{\mathbf{A}}_{\mathbf{h}} \odot (\tilde{\mathbf{E}}_{\mathbf{ref_h}} \mathbf{K_h})\right)_{\mathbf{m}}$ in relation with the number of pixels of the multispectral image and the scale factor between it and the number of pixels of the hyperspectral image.

4.1.4. Process 4: Fusion

Finally, the unobservable sharpened high-spectral/high-spatial resolution hyperspectral image $\tilde{\mathbf{X}}_{\mathbf{f}} \in \mathbb{R}_{+}^{L_h \times P_m}$ is obtained by combining two matrix variables: the hyperspectral spectra matrix $\left(\tilde{\mathbf{A}}_{\mathbf{h}} \odot (\tilde{\mathbf{E}}_{\mathbf{ref_h}} \mathbf{K_h})\right)_{\mathbf{m}} \in \mathbb{R}_{+}^{L_h \times (P_m M)}$ with a high spectral resolution, resulting from the hyperspectral unmixing process (Process 1) and resizing process (Process 3), and the multispectral abundance maps $\tilde{\mathbf{C}}'_{\mathbf{s_m}} \in \mathbb{R}_{+}^{(P_m M) \times P_m}$ with a high spatial resolution obtained by multispectral unmixing process (Process 2) and resizing process (Process 3). The following expression illustrates this combination.

$$\tilde{\mathbf{X}}_{\mathbf{f}} = \left(\tilde{\mathbf{A}}_{\mathbf{h}} \odot (\tilde{\mathbf{E}}_{\mathbf{ref_h}} \mathbf{K_h})\right)_{\mathbf{m}} \tilde{\mathbf{C}}'_{\mathbf{s_m}}. \tag{12}$$

4.2. Proposed unmixing-based fusion algorithm

The designed NMF-unmixing-based fusion algorithm that deals with spectral variability when processing hyperspectral data operates in three distinct steps, which are described in the following subsections.

4.2.1. The initialisation step

This step aims to initialise the different varying matrices involved in the proposed algorithm. Indeed, the designed fusion approach is an NMF-unmixing-based method, and like standard linear NMF-based methods, is not guaranteed to provide a unique solution and its convergence point depends on its initialisation. Thus, to avoid a random initialisation of each varying matrix, the following strategy is adopted: the well-known Vertex Component Analysis (VCA) technique (J.M.P. Nascimento and Dias 2005) is used to estimate an initial M-reference hyperspectral endmember spectra matrix $\tilde{\mathbf{E}}_{\mathbf{ref_h}}^{(\mathbf{0})}$ from the observed matrix $\mathbf{X_h}$. This matrix is then used to estimate an initial M-multispectral endmember spectra matrix $\tilde{\mathbf{E}}_{\mathbf{ref_m}}^{(\mathbf{0})}$ (by employing the Spectral Response Function (SRF) of the considered multispectral sensor). Moreover, $\tilde{\mathbf{E}}_{\mathbf{ref_h}}^{(\mathbf{0})}$ is also used to estimate initial low spatial resolution abundance fractions by means of the Fully Constrained Least Squares (FCLS) (Heinz and Chang 2001) method, separately applied to each pixel of the hyperspectral image. These abundance fractions are then reorganized as in (6) to form the initial estimated low spatial resolution abundance fractions matrix $\tilde{\mathbf{C}}_{\mathbf{h}}^{(\mathbf{0})}$. In the same way is formed the initial estimated high spatial resolution abundance fractions matrix $\tilde{\mathbf{C}}_{\mathbf{s_m}}^{(\mathbf{0})}$ by means of the FCLS technique, separately applied, by considering $\tilde{\mathbf{E}}_{\mathbf{ref_m}}^{(\mathbf{0})}$, to each pixel of the multispectral image.

4.2.2. The optimisation step

In this investigation, the proposed fusion approach aims to generate an unobservable high spectral and spatial resolution hyperspectral image $\tilde{\mathbf{X}}_{\mathbf{f}} \in \mathbb{R}_{+}^{L_h \times P_m}$ by alternately unmixing $\mathbf{X_h}$ and $\mathbf{X_m}$ images using the multiplicative CNMF algorithm described in (Yokoya, Yairi, and

Iwasaki 2012) but by replacing the varying matrices of (Yokoya, Yairi, and Iwasaki 2012) by those with the specific structures described above, which are relevant for addressing the spectral variability phenomenon (see Processes 1 and 2 in Section 4.1) when processing the hyperspectral data. Also, it is useful to remind that the designed algorithm exploits a spatial degradation model between the considered two datasets (see Process 3 in Section 4.1).

In the proposed method, an external loop is used, wherein the hyperspectral and multispectral varying matrices are alternately updated through the use of two inner loops. In the first inner loop, the hyperspectral varying matrices are updated, in order to minimize J_1 defined by (10), using gradient-based iterative and multiplicative update rules. Using the properties in (Petersen and Pedersen 2012), it may be shown that the gradient expressions, in matrix form, of J_1 are

$$\frac{\partial \mathrm{J}_1}{\partial \widetilde{\mathbf{A}}_{\mathbf{h}}} = \left(\left(\widetilde{\mathbf{A}}_{\mathbf{h}} \odot (\tilde{\mathbf{E}}_{\mathbf{ref_h}} \mathbf{K}_{\mathbf{h}})\right) \tilde{\mathbf{C}}_{\mathbf{h}} \tilde{\mathbf{C}}_{\mathbf{h}}^{\mathbf{T}} - \mathbf{X}_{\mathbf{h}} \tilde{\mathbf{C}}_{\mathbf{h}}^{\mathbf{T}}\right) \odot (\tilde{\mathbf{E}}_{\mathbf{ref_h}} \mathbf{K}_{\mathbf{h}}) - \alpha(\mathbf{1}^{L_h \times MP_h} - \widetilde{\mathbf{A}}_{\mathbf{h}}), \tag{13}$$

$$\frac{\partial \mathrm{J}_1}{\partial \tilde{\mathbf{E}}_{\mathbf{ref_h}}} = \left(\left(\left(\widetilde{\mathbf{A}}_{\mathbf{h}} \odot (\tilde{\mathbf{E}}_{\mathbf{ref_h}} \mathbf{K}_{\mathbf{h}})\right) \tilde{\mathbf{C}}_{\mathbf{h}} \tilde{\mathbf{C}}_{\mathbf{h}}^{\mathbf{T}}\right) \odot \widetilde{\mathbf{A}}_{\mathbf{h}} - \left(\mathbf{X}_{\mathbf{h}} \tilde{\mathbf{C}}_{\mathbf{h}}^{\mathbf{T}}\right) \odot \widetilde{\mathbf{A}}_{\mathbf{h}}\right) \mathbf{K}_{\mathbf{h}}^{\mathbf{T}}, \tag{14}$$

$$\frac{\partial \mathrm{J}_1}{\partial \tilde{\mathbf{C}}_{\mathbf{h}}} = \left(\widetilde{\mathbf{A}}_{\mathbf{h}} \odot (\tilde{\mathbf{E}}_{\mathbf{ref_h}} \mathbf{K}_{\mathbf{h}})\right)^{\mathrm{T}} \left(\left(\widetilde{\mathbf{A}}_{\mathbf{h}} \odot (\tilde{\mathbf{E}}_{\mathbf{ref_h}} \mathbf{K}_{\mathbf{h}})\right) \tilde{\mathbf{C}}_{\mathbf{h}} - \mathbf{X}_{\mathbf{h}}\right). \tag{15}$$

Since the proposed algorithm is a multiplicative one, the procedure described in (Benhalouche, Karoui, and Deville 2019), for deriving iterative update rules, is applied. Thus, the above gradient expressions result in the following multiplicative update rules

$$\begin{gathered} \widetilde{\mathbf{A}}_{\mathbf{h}} \leftarrow \widetilde{\mathbf{A}}_{\mathbf{h}} \odot \left(\left(\left(\mathbf{X}_{\mathbf{h}} \tilde{\mathbf{C}}_{\mathbf{h}}^{\mathbf{T}}\right) \odot \left(\tilde{\mathbf{E}}_{\mathbf{ref_h}} \mathbf{K}_{\mathbf{h}}\right)\right) + \alpha \times \mathbf{1}^{L_h \times MP_h}\right) \\ \oslash \left(\left(\left(\widetilde{\mathbf{A}}_{\mathbf{h}} \odot (\tilde{\mathbf{E}}_{\mathbf{ref_h}} \mathbf{K}_{\mathbf{h}})\right) \tilde{\mathbf{C}}_{\mathbf{h}} \tilde{\mathbf{C}}_{\mathbf{h}}^{\mathbf{T}}\right) \odot (\tilde{\mathbf{E}}_{\mathbf{ref_h}} \mathbf{K}_{\mathbf{h}}) + \alpha \widetilde{\mathbf{A}}_{\mathbf{h}} + \varepsilon\right), \end{gathered} \tag{16}$$

$$\begin{aligned}\tilde{\mathbf{E}}_{\mathbf{ref_h}} \leftarrow \tilde{\mathbf{E}}_{\mathbf{ref_h}} \odot \left(\left(\left(\mathbf{X_h}\tilde{\mathbf{C}}_{\mathbf{h}}^{\mathbf{T}}\right) \odot \tilde{\mathbf{A}}_{\mathbf{h}}\right) \mathbf{K_h}^{\mathbf{T}}\right) \\ \oslash \left(\left(\left((\tilde{\mathbf{A}}_{\mathbf{h}} \odot (\tilde{\mathbf{E}}_{\mathbf{ref_h}}\mathbf{K_h}))\tilde{\mathbf{C}}_{\mathbf{h}}\tilde{\mathbf{C}}_{\mathbf{h}}^{\mathbf{T}}\right) \odot \tilde{\mathbf{A}}_{\mathbf{h}}\right) \mathbf{K_h}^{\mathbf{T}} + \varepsilon\right),\end{aligned} \tag{17}$$

$$\begin{aligned}\tilde{\mathbf{C}}_{\mathbf{h}} \leftarrow \tilde{\mathbf{C}}_{\mathbf{h}} \odot \left(\left(\tilde{\mathbf{A}}_{\mathbf{h}} \odot \left(\tilde{\mathbf{E}}_{\mathbf{ref_h}}\mathbf{K_h}\right)\right)^{\mathrm{T}} \mathbf{X_h}\right) \\ \oslash \left((\tilde{\mathbf{A}}_{\mathbf{h}} \odot (\tilde{\mathbf{E}}_{\mathbf{ref_h}}\mathbf{K_h}))^{\mathrm{T}}(\tilde{\mathbf{A}}_{\mathbf{h}} \odot \tilde{\mathbf{E}}_{\mathbf{ref_h}}\mathbf{K_h})\tilde{\mathbf{C}}_{\mathbf{h}} + \varepsilon\right),\end{aligned} \tag{18}$$

where $\oslash$ corresponds to element-wise division and ε (very small and positive value) is considered to avoid possible division by zero.

Subsequently, the spectral variable $\tilde{\mathbf{E}}_{\mathbf{ref_h}}$ (i.e., reference hyperspectral endmember spectra) obtained by using the update rule (17) is spectrally down-sampled by means of the SRF of the considered multispectral sensor, and the obtained $\tilde{\mathbf{E}}_{\mathbf{ref_m}}$ is then used in the second inner loop.

In the second inner loop, the multispectral varying matrices are updated, in order to minimize J_2 defined by (11), using iterative and multiplicative update rules. These rules use the gradient expressions of J_2, which are in matrix form

$$\frac{\partial \mathrm{J}_2}{\partial \tilde{\mathbf{E}}_{\mathbf{ref_m}}} = \tilde{\mathbf{E}}_{\mathbf{ref_m}}\tilde{\mathbf{C}}_{\mathbf{s_m}}\tilde{\mathbf{C}}_{\mathbf{s_m}}^{\mathbf{T}} - \mathbf{X_m}\tilde{\mathbf{C}}_{\mathbf{s_m}}^{\mathbf{T}}, \tag{19}$$

$$\frac{\partial \mathrm{J}_2}{\partial \tilde{\mathbf{C}}_{\mathbf{s_m}}} = \tilde{\mathbf{E}}_{\mathbf{ref_m}}^{\mathbf{T}}\tilde{\mathbf{E}}_{\mathbf{ref_m}}\tilde{\mathbf{C}}_{\mathbf{s_m}} - \tilde{\mathbf{E}}_{\mathbf{ref_m}}^{\mathbf{T}}\mathbf{X_m}. \tag{20}$$

Thus, the following iterative and multiplicative update rules are obtained

$$\tilde{\mathbf{E}}_{\mathbf{ref_m}} \leftarrow \tilde{\mathbf{E}}_{\mathbf{ref_m}} \odot \left(\mathbf{X_m}\tilde{\mathbf{C}}_{\mathbf{s_m}}^{\mathbf{T}}\right) \oslash \left(\tilde{\mathbf{E}}_{\mathbf{ref_m}}\tilde{\mathbf{C}}_{\mathbf{s_m}}\tilde{\mathbf{C}}_{\mathbf{s_m}}^{\mathbf{T}} + \varepsilon\right), \tag{21}$$

$$\tilde{\mathbf{C}}_{\mathbf{s_m}} \leftarrow \tilde{\mathbf{C}}_{\mathbf{s_m}} \odot \left(\tilde{\mathbf{E}}^{\mathbf{T}}_{\mathbf{ref_m}} \mathbf{X_m}\right) \oslash \left(\tilde{\mathbf{E}}^{\mathbf{T}}_{\mathbf{ref_m}} \tilde{\mathbf{E}}_{\mathbf{ref_m}} \tilde{\mathbf{C}}_{\mathbf{s_m}} + \varepsilon\right). \tag{22}$$

For the varying matrix $\tilde{\mathbf{C}}_{\mathbf{s_m}}$, in addition to the update rule (22), the constraint of the abundance sum-to-one (Heinz and Chang 2001), expressed below, is considered: each element of a column of $\tilde{\mathbf{C}}_{\mathbf{s_m}}$ is divided by the sum of element values of that column

$$\left[\tilde{c}_{s_{m_{1,i}}}, \dots, \tilde{c}_{s_{m_{M,i}}}\right] \leftarrow \left[\tilde{c}_{s_{m_{1,i}}}, \dots, \tilde{c}_{s_{m_{M,i}}}\right] / \textstyle\sum_{j=1}^{M} \tilde{c}_{s_{m_{j,i}}}. \tag{23}$$

The high spatial resolution abundance fractions (i.e., $\tilde{\mathbf{C}}_{\mathbf{s_m}} \in \mathbb{R}_{+}^{M \times P_m}$), obtained by using the update rules (22) and (23), are then spatially down-sampled by means of, for instance, the Point Spread Function (PSF) of the hyperspectral sensor. This results in the matrix $\tilde{\mathbf{C}}_{\mathbf{s_{md}}} \in \mathbb{R}_{+}^{M \times P_h}$. This operation may be performed according to the following expression

$$\tilde{\mathbf{C}}_{\mathbf{s_{md}}} = \tilde{\mathbf{C}}_{\mathbf{s_m}} \mathbf{D}, \tag{24}$$

where $\mathbf{D} \in \mathbb{R}_{+}^{P_m \times P_h}$ is a linear operator, which performs spatial degradation between multispectral and hyperspectral data. This operator can be seen as a blurring-decimation matrix and spatial down-sampling factor that is a block-diagonal sparse matrix having Gaussian filter values (Borsoi et al. 2021; Sun et al. 2024). $\tilde{\mathbf{C}}_{\mathbf{s_{md}}}$ is then restructured, as described in (6), to obtain $\tilde{\mathbf{C}}_{\mathbf{h}} \in \mathbb{R}_{+}^{(P_h M) \times P_h}$, which is then used, in the next iteration of the outer loop, in the first inner loop. It is important to mention here that the above rules (16), (17) and (18), which are the update rules of the hyperspectral varying matrices, remain pertinent for addressing the spectral variability phenomenon when all the elements of $\tilde{\mathbf{C}}_{\mathbf{h}}$, which correspond to zero-valued elements in (6) are initially set to zero: as the new value of each such element in (18) is made equal to the product of its previous value by another factor, it thus remains equal to zero throughout all updates, as required by the specific structure of (6), whereas the other elements of $\tilde{\mathbf{C}}_{\mathbf{h}}$ and the complete matrices $\tilde{\mathbf{A}}_{\mathbf{h}}$ and $\tilde{\mathbf{E}}_{\mathbf{ref_h}}$ are updated according to the same principle as in (Benhalouche, Karoui, and Deville 2019).

Also, the proposed alternating unmixing processes are stopped when the numbers of iterations, of the outer and inner loops, reach predefined maximum values.

Note that once the optimisation process has been achieved, the final obtained version of the matrix $\tilde{\mathbf{C}}_{\mathbf{s_m}} \in \mathbb{R}_+^{M \times P_m}$ is reorganised as a block-diagonal matrix in order to obtain the matrix $\tilde{\mathbf{C}}'_{\mathbf{s_m}} \in \mathbb{R}_+^{(P_m M) \times P_m}$ (see Process 3 in Section 4.1), that will subsequently be used in the fusion step.

4.2.3. The fusion step

This final step of the proposed approach consists in deriving the unobservable sharpened high spatial and spectral resolution hyperspectral image $\tilde{\mathbf{X}}_{\mathbf{f}}$ by recombining the obtained high spatial resolution abundance fractions and hyperspectral endmember spectra matrices, by using (12) and after obtaining the final estimates of $\left(\tilde{\mathbf{A}}_{\mathbf{h}} \odot (\tilde{\mathbf{E}}_{\mathbf{ref_h}} \mathbf{K}_{\mathbf{h}})\right)_{\mathbf{m}}$ and $\tilde{\mathbf{C}}'_{\mathbf{s_m}}$ (calculated as described in Section 4.1.4).

The complete pseudo-code and the graphical diagram of the designed fusion algorithm, called Extended CNMF to address spectral Variability, and denoted Ext-CNMF-Var are provided below.

```
Algorithm 1: Ext-CNMF-Var fusion algorithm.
Input: High spectral resolution hyperspectral image $\mathbf{X_h}$ and high spatial resolution multispectral image $\mathbf{X_m}$.

1. Determine the number $M$ of endmembers.

2. The initialisation step
    2.a. Initialise $\tilde{\mathbf{E}}^{(\mathbf{0})}_{\mathbf{ref_h}}$ from $\mathbf{X_h}$ by using the VCA method.
    2.b. Initialise $\tilde{\mathbf{C}}^{(\mathbf{0})}_{\mathbf{h}}$ from $\mathbf{X_h}$ and initial $\tilde{\mathbf{E}}^{(\mathbf{0})}_{\mathbf{ref_h}}$ by using the FCLS method and then reorganise it as in (6).
    2.c. Initialise $\widetilde{\mathbf{A}}^{(\mathbf{0})}_{\mathbf{h}}$ with a unit matrix $\mathbf{1} \in \mathbb{R}_+^{L_h \times (P_h M)}$.
    2.d. Initialise $\tilde{\mathbf{E}}^{(\mathbf{0})}_{\mathbf{ref_m}}$ from initial $\tilde{\mathbf{E}}^{(\mathbf{0})}_{\mathbf{ref_h}}$.
    2.e. Initialise $\tilde{\mathbf{C}}^{(\mathbf{0})}_{\mathbf{s_m}}$ from $\mathbf{X_m}$ and initial $\tilde{\mathbf{E}}^{(\mathbf{0})}_{\mathbf{ref_m}}$ by using the FCLS method.
3. The optimisation step
An external loop (over substeps 3.a. to 3.d.) in which the hyperspectral and multispectral varying matrices are alternately updated using two inner loops.
    3.a. First inner loop
        Repeatedly perform the following substeps:
        − Optimise $\widetilde{\mathbf{A}}_{\mathbf{h}}$ by using (16).
        − Optimise $\tilde{\mathbf{E}}_{\mathbf{ref_h}}$ by using (17).
        − Optimise $\tilde{\mathbf{C}}_{\mathbf{h}}$ by using (18).
    3.b. $\tilde{\mathbf{E}}_{\mathbf{ref_h}}$ is spectrally down-sampled, using the SRF of the considered multispectral sensor, to obtain $\tilde{\mathbf{E}}_{\mathbf{ref_m}}$ that is then used in the second inner loop.
    3.c. Second inner loop
        Repeatedly perform the following substeps:
        − Optimise $\tilde{\mathbf{E}}_{\mathbf{ref_m}}$ by using (21).
        − Optimise $\tilde{\mathbf{C}}_{\mathbf{s_m}}$ by using (22) and (23).
    3.d. $\tilde{\mathbf{C}}_{\mathbf{s_m}}$ is spatially down-sampled by using (24), and then restructured using (6) to obtain $\tilde{\mathbf{C}}_{\mathbf{h}}$, which is, then, used in the next iteration of the first inner loop.
4. The Fusion step
    4.a. Restructure $\tilde{\mathbf{C}}_{\mathbf{s_m}}$, as in (6), to obtain $\tilde{\mathbf{C}}'_{\mathbf{s_m}}$.
    4.b. Resize the matrix product $\big(\widetilde{\mathbf{A}}_{\mathbf{h}} \odot (\tilde{\mathbf{E}}_{\mathbf{ref_h}} \mathbf{K_h})\big)$ to $\big(\widetilde{\mathbf{A}}_{\mathbf{h}} \odot (\tilde{\mathbf{E}}_{\mathbf{ref_h}} \mathbf{K_h})\big)_{\mathbf{m}}$.
    4.c. Fuse obtained high-spectral hyperspectral and high-spatial multispectral matrix variables using (12).
Output: Unobservable sharpened high-spectral/high-spatial resolution hyperspectral image $\widetilde{\mathbf{X}}_{\mathbf{f}}$.
```

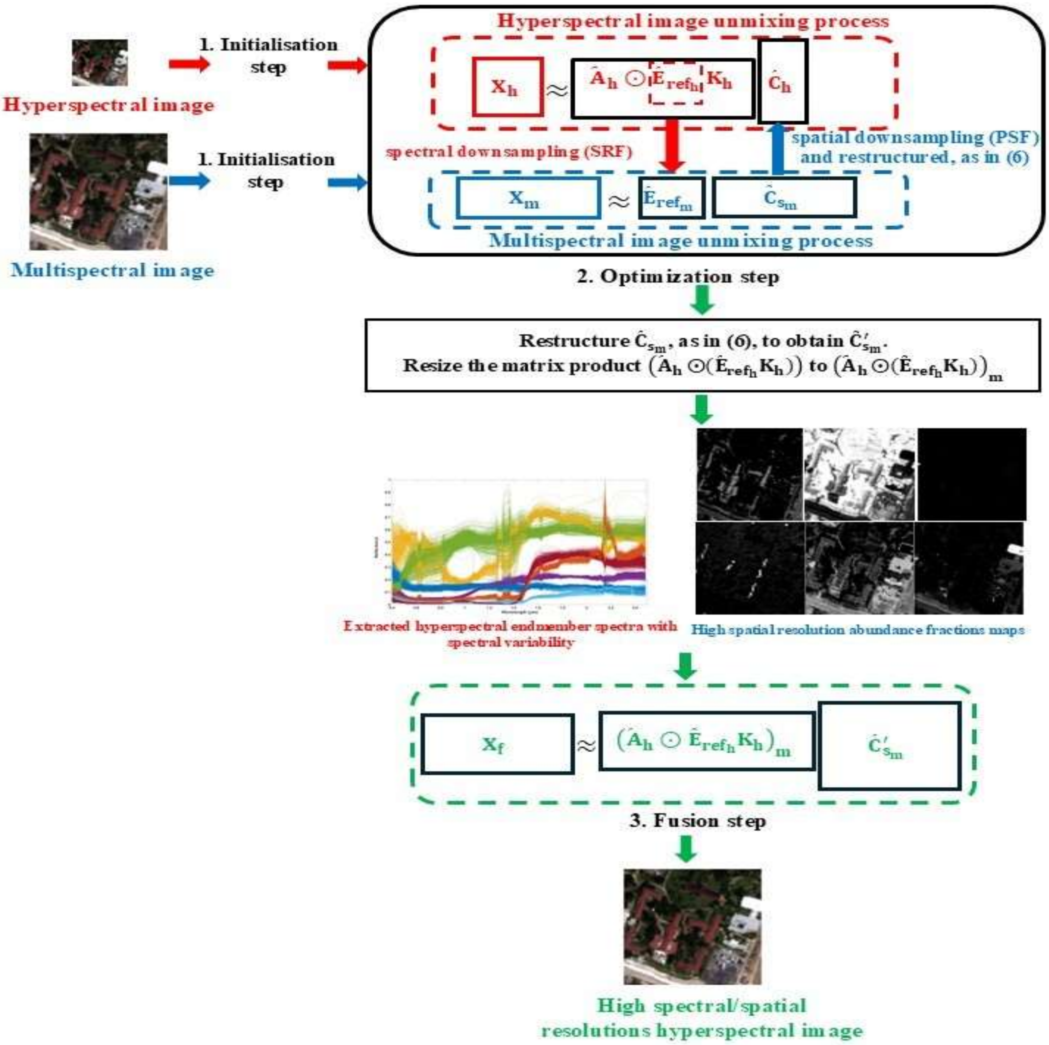

Figure 1. Graphical diagram of the designed Ext-CNMF-Var fusion algorithm.

5. Tested data

In this section, the used synthetic and real datasets are described. These datasets are used to evaluate the performance of the proposed fusion approach, and the obtained results are then compared to those obtained by other approaches from the literature.

5.1. Synthetic data

The experiments are first conducted using three synthetic datasets.

The first considered synthetic dataset is extracted from the real airborne hyperspectral image with high spatial and spectral resolutions described in (Brezini et al. 2022). More precisely, a subset of this real hyperspectral image, involving 7 classes of endmembers (grass, tree, soil, residential, commercial, road and parking areas) with spectral variability, is considered to conduct first experiments. This real image subset of 100×100-pixels, with 144 wavelengths covering the 0.38-1.05 µm spectral range, is used as a reference hyperspectral image (Figure 2(a)) and is considered, using Wald's protocol (Wald 1997), to generate two synthetic sub-datasets. Indeed, by means of Wald's protocol, this image is spatially degraded, by a scale factor of 2 (respectively 4), using a Gaussian filter (which can be seen as the PSF of the considered hyperspectral sensor) to generate the hyperspectral image with a low spatial resolution (Karoui et al. 2017). The multispectral image with a low spectral resolution, with 5 (respectively 8) spectral bands, is obtained by spectrally down-sampling the reference hyperspectral image using the SRF of the Landsat-8 Operational Land Imager (OLI) (respectively WorldView-3) sensor, considering only the first 5 (respectively 8) bands covering the spectral range 0.43-0.88 µm (respectively 0.40-1.04 µm). Thus, the first sub-dataset consists of a 100×100-pixel reference hyperspectral image with 144 spectral bands, a 50×50-pixel low spatial resolution hyperspectral image with 144 spectral bands, and a 100×100-pixel high spatial resolution multispectral image with 5 spectral bands. The second sub-dataset consists of a 100×100-pixel reference hyperspectral image with 144 spectral bands, a 25×25-pixel low spatial resolution hyperspectral image with 144 spectral bands, and a 100×100-pixel high spatial resolution multispectral image with 8 spectral bands.

The second synthetic dataset contains a part of the real hyperspectral image acquired over the University of Houston campus, Texas, USA, in June 2012 (Figure 2(b)), which was used in the 2013 IEEE GRSS Data Fusion Contest (DFC) (Debes et al. 2014). This real image was acquired over the Robertson stadium and is composed of 105×126 pixels with 144 spectral bands ranging from 0.38 µm to 1.05 µm. It mainly consists of four materials: vegetation, asphalt, metal roofing and concrete (Figure 2(b)). By means of Wald's protocol, this synthetic image is spatially degraded, by a scale factor of 3, by applying a spatial Gaussian filter (Karoui et al. 2017) to generate the hyperspectral image with a low spatial resolution. The multispectral image with a low spectral resolution (4 spectral bands covering the spectral range 0.46-0.88 μm) is obtained by spectrally down-sampling the reference hyperspectral image using the SRF of the Sentinel-2 sensor (by considering its spectral bands: 2, 3, 4, and 8). Therefore, this second synthetic dataset includes a 105×126-pixel reference hyperspectral image with 144 spectral bands, a 35×42-pixel low spatial resolution hyperspectral image with 144 spectral bands, and a 105×126-pixel multispectral high spatial resolution image with 4 spectral bands.

The third considered synthetic dataset is derived from the real hyperspectral Urban data (Figure 2(c)) used in (Zhu et al. 2014). This image, which is one of the most used datasets for classification, hyperspectral unmixing, or sharpening of hyperspectral images, was acquired by the HYperspectral Digital Imagery Collection Experiment (HYDICE) sensor over the Copperas Cove, near Fort Hood, Texas, USA. This 307×307-pixel hyperspectral image, with a 2-m spatial resolution, contains 162 spectral bands (after removing the water absorption bands from the 210 spectral bands of the original data) ranging from 0.4 to 2.5 μm. In this work, a part of this image containing 256 × 256 pixels, mainly composed of asphalt, grass, tree, and roof, is used and considered as the reference hyperspectral image, which is subsequently spatially degraded, by a scale factor of 2, by applying a spatial Gaussian filter (Karoui et al. 2017) to generate the hyperspectral image with a low spatial resolution. The multispectral image, with a low spectral resolution (4 spectral bands covering the spectral range 0.45-0.9 μm), is obtained by spectrally down-sampling the reference hyperspectral image using the SRF of the QuickBird sensor.

In addition, white Gaussian noise with a signal-to-noise ratio (SNR) of 35 dB (respectively 40 dB) is added to each generated low spatial resolution hyperspectral dataset (respectively each generated high spatial resolution multispectral image).

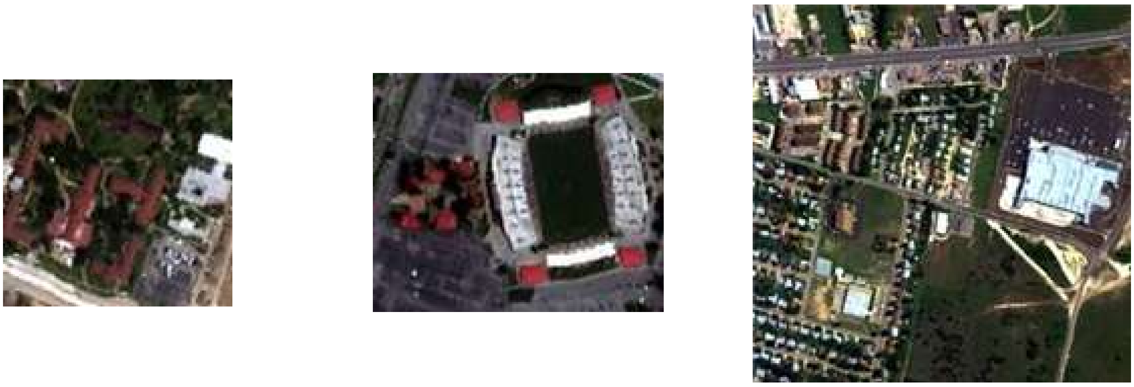

(a) (b) (c)

Figure 2. True-color image composite of considered real hyperspectral images from which synthetic data are created: (a) image described in (Brezini et al. 2022), (b) Houston image (Debes et al. 2014) and (c) Urban data (Zhu et al. 2014).

5.2. Real data

In these investigations, two real data are also tested. The first considered real data (radiometrically and geometrically corrected), are acquired on the same day (March 3, 2003) and at the same time, and cover a part of the urban area of Oran, Algeria. The high spectral resolution hyperspectral image (Figure 3(a)) was acquired by the Earth Observing-1 (EO-1) Hyperion sensor. This image has a spatial resolution of 30 m, involves 7 classes, and contains 125 spectral bands (after removing spectral bands with a low signal-to-noise ratio). The high spatial resolution pansharpened multispectral image (Figure 3(b)) is provided by the EO-1 Advanced Land Imager (ALI) sensor, with a spatial resolution of 10 m and 9 spectral bands.

(a) (b)

Figure 3. True-color image composite of the first tested real data: (a) low spatial resolution hyperspectral image (EO-1 Hyperion sensor), (b) high spatial resolution pansharpened multispectral image (EO-1 ALI sensor).

The second considered real data (radiometrically and geometrically corrected), cover a part of the North-Eastern urban area of Oran, Algeria. The used hyperspectral data (Figure 4(a)) are those acquired by the PRISMA spaceborne sensor on September 7, 2024. This image includes 10 classes, with a spatial resolution of 30 m, 234 spectral bands in the visible and near-infrared (VNIR) (63 bands), and short-wave infrared (SWIR) (171 bands) regions. Among these 234 spectral bands, only 103 (46 covering the spectral range from 475.32 to 913.45 nm in the VNIR domain and 57, from 1029.35 to 2298.61 nm, in the SWIR region) are taken into account, while the other bands are ignored due to the presence of noise or atmospheric absorption windows. The used multispectral image (Figure 4 (b)), with a high spatial resolution, is the one provided by the Sentinel-2 satellite and acquired on September 10, 2024, where only spectral bands 2, 3, 4 and 8 with a spatial resolution of 10 m are considered.

(a) (b)

Figure 4. True-color image composite of the second tested real data: (a) low spatial resolution hyperspectral image (PRISMA sensor), (b) high spatial resolution multispectral image (Sentinel-2 sensor).

6. Experimental results

6.1. Performance evaluation criteria

In this subsection, used performance evaluation criteria are described. Two categories of criteria are considered (Wald 2000; Restaino et al. 2020):

6.1.1. *Reference-based reduced-resolution assessment*

According to Wald’s protocol (Wald 1997), the reduced-resolution evaluation involves measuring the similarity between the fused image and an ideal reference one. Thus, when considering synthetic data, the performance of the proposed NMF-unmixing-based fusion approach that deals with spectral variability, and that of the tested approaches from the literature, are evaluated by comparing the estimated unobservable high-spectral/high-spatial resolution sharpened images with the reference hyperspectral image. To this end, there are several criteria. The most used and considered in this investigation are the Spectral Angle Mapper (SAM) and the Spectral Information Divergence (SID). These criteria are calculated between each pixel spectrum in the reference hyperspectral image and its analogue in the estimated image. Smaller values of these criteria indicate a better spectral reconstruction quality. Furthermore, the Structural SIMilarity (SSIM) index, with an efficiency range typically between 0 and 1, the Peak Signal to Noise Ratio (PSNR), and the Relative Dimensionless Global Error in Synthesis (ERGAS: French acronym for "Erreur Relative Globale Adimensionnelle de Synthèse") (Yokoya, Grohnfeldt, and Chanussot 2017) are also used in this investigation. These criteria are calculated between each spectral band in the reference hyperspectral image and its analogue in the estimated one. Smaller ERGAS values indicate a better reconstruction quality. Higher SSIM and PSNR values correspond to the best reconstruction quality.

6.1.2. *Non-reference-based full-resolution assessment*

For experiments with real data, when reference hyperspectral images are unavailable, the evaluation is based on the full-resolution assessment procedure by using non-reference-based assessment criteria. This includes the modified Quality with No Reference (mQNR) criterion, described in (Alparone et al. 2008; Karoui et al. 2017; Xu and Ehlers 2022). This criterion reads

$$\mathrm{mQNR} = (1 - \mathrm{D}_{\lambda})^{\sigma}(1 - \mathrm{D}_{\mathrm{s}})^{\rho}, \tag{25}$$

where σ and ρ are real-valued exponents (set to 1 in the conducted experiments), and D_{λ} and D_{s} are, respectively, spectral and spatial distortion indices. The spectral distortion index reads

$$\mathrm{D}_{\lambda} = \sqrt[\omega]{\frac{1}{\mathrm{L_h}(\mathrm{L_h}-1)} \sum_{\mathrm{j}=1}^{\mathrm{L_h}} \sum_{\mathrm{r}=1,\mathrm{r}\neq \mathrm{j}}^{\mathrm{L_h}} \left|\mathrm{UIQI}\left(\mathrm{X}_{\mathrm{f_j}}, \mathrm{X}_{\mathrm{f_r}}\right) - \mathrm{UIQI}(\mathrm{X}_{\mathrm{h_j}}, \mathrm{X}_{\mathrm{h_r}})\right|^{\omega}}, \tag{26}$$

where ω is a positive integer exponent (set to 1 in the conducted experiments). $\mathbf{X}_{\mathbf{f}_{.}}$ is one spectral band of the sharpened image. $\mathbf{X}_{\mathbf{h}_{.}}$ is one spectral band of the hyperspectral image (Alparone et al. 2008). The spatial distortion index D_{s} is calculated as follows: for each spectral band of the multispectral image, a spatial distortion sub-index is calculated, by using the standard index, defined in (Alparone et al. 2008), between the considered multispectral band and hyperspectral bands that are covered by the considered multispectral range. The final spatial distortion index D_{s} represents the mean of the calculated sub-indices (Karoui et al. 2017). These two distortion indices use the Universal Image Quality Index (UIQI) (Zhou Wang and Bovik 2002). The ranges of mQNR, D_{λ}, and D_{s} are [0, 1]. A higher mQNR value indicates a higher spatial-spectral reconstruction quality. A smaller spectral (respectively spatial) distortion value indicates a better spectral (respectively spatial) reconstruction.

6.2. Obtained results

Experiments are carried out with the datasets defined above to evaluate the performance of the proposed Ext-CNMF-Var fusion method. The obtained results are also compared to those of methods from the literature. A first category of unsupervised methods addresses spectral variability and includes the method proposed in (Benhalouche et al. 2022), here called CNMF-Var, the method proposed in (Karoui et al. 2021), here called Multi-JCNMF-Var, the HMF-IPNMF method (Brezini et al. 2022), the FuVar approach (Borsoi, Imbiriba, and Bermudez 2020), the unmixing-based FSVA method, which uses the ALMM model to include spectral variability in the modelling process and exploits the ADMM optimisation algorithm (Camacho, Vargas, and Arguello 2022), and the DL-based DIFIV (Deep hyperspectral and multispectral Image Fusion with Inter-image Variability) method (Wang et al. 2023). The second category includes unsupervised methods that do not deal with the spectral variability phenomenon, namely the CNMF (Yokoya, Yairi, and Iwasaki 2012) one, the HySure (Simoes et al. 2015) technique, and the SFIM (J. G. Liu 2000) method. CNMF and HySure are two methods based on the matrix decomposition concept, which do not take the spectral variability phenomenon into account. Therefore, these methods are applied by considering two scenarios: in the first scenario (scenario (a)), these methods are executed by using a number of endmember classes equal to M, whereas in the second one (scenario (b)), they are applied by considering the number provided by the Hyperspectral Signal subspace Identification by Minimum Error (HySime) (Bioucas-Dias et al. 2012) method.

The maximum number of iterations, used in each of the two inner loops of the Ext-CNMF-Var method (as for the CNMF-Var and CMNF methods), is set to 100, while the maximum number of iterations of the outer loop is set to 3. For the HMF-IPNMF and Multi-JCNMF-Var methods, the maximum number of iterations is set to 100, and the regularization parameter for HMF-IPNMF, is set to 30. For the FuVar, FSVA, DIVIF, HySure and SFIM methods, the parameters of these algorithms are set according to the original works described in (Simoes et al. 2015; Camacho, Vargas, and Arguello 2022; Wang et al. 2023; Borsoi, Imbiriba, and Bermudez 2020; Liu 2000). In addition, the spatial and spectral degradation operators are assumed to be known as a priori for the HySure, CNMF and FuVar methods.

The CPU used in the conducted experiments is an Intel® Core™ i7-1260P, 2.10 GHz, with a memory capacity of 16 GB. The computational costs and averages of the spectral and spatial criteria of the tested methods are shown hereafter.

6.2.1. *Choosing the initialisation procedure*

As mentioned above, and since the proposed fusion approach is an NMF-based method, it is not guaranteed to provide a unique solution, and its convergence point depends on its initialisation. Therefore, in order to avoid a random initialisation of the hyperspectral and multispectral matrix variables considered in the proposed fusion approach, three endmember spectra extraction techniques, namely VCA (Nascimento and Dias 2005), SGA (Chang et al. 2010) and N-FINDER (Winter 1999), combined either with a Uniform distribution of abundances or abundance values estimated by FCLS, are tested, on the first sub-dataset generated from the first considered synthetic dataset, as initialisation points of the designed fusion approach. This investigation is performed successively with two values of the spectral variability regularisation/penalisation coefficient α, that is: 1) $\alpha = 1$, chosen to give equal weights to the two terms defined in (10), and 2) $\alpha = 10^{-3}$, chosen after a sensitivity analysis described hereafter in Subsection 6.2.2. These tests allow, on the one hand, some assessment of the initialisation impact on the sharpened data qualities, and on the other hand, an evaluation of the robustness of the proposed fusion approach with respect to different initialisation points.

The performances, of the designed fusion method, obtained with these initialisation strategies are presented in Tables I and II.

Table I. Obtained performance values, of the designed fusion method, for the first sub-dataset generated from the first considered synthetic dataset, with different initialisation strategies and the coefficient α set to 1 (the bold values correspond to the best performances, and the italic underlined ones correspond to the second-best performances).

Method	**Ideal value**	**VCA +Uniform**	**VCA +FCLS**	**SGA +Uniform**	**SGA +FCLS**	**N-FINDR +Uniform**	**N-FINDR +FCLS**
SAM (°)	0	10.59	**1.90**	10.47	2.94	10.67	*2.07*
SID	0	4.61	**0.08**	4.66	0.93	4.59	*0.18*
SSIM	1	0.4335	**0.9834**	*0.4017*	0.8814	0.4383	*0.9686*
PSNR (dB)	∞	19.98	**41.82**	19.86	25.53	20.04	*36.41*
ERGAS	0	28.03	*4.47*	28.44	15.00	27.84	**4.42**

Table II. Obtained performance values, of the designed fusion method, for the first sub-dataset generated from the first considered synthetic dataset, with different initialisation strategies and the coefficient α set to 10^{-3} (the bold values correspond to the best performances, and the italic underlined ones correspond to the second-best performances).

Method	**Ideal value**	**VCA +Uniform**	**VCA +FCLS**	**SGA +Uniform**	**SGA +FCLS**	**N-FINDR +Uniform**	**N-FINDR +FCLS**
SAM (°)	0	9.99	**1.62**	10.29	2.47	9.97	*1.87*
SID	0	4.52	**0.10**	5.01	0.87	4.49	0.17
SSIM	1	0.4634	**0.9787**	0.4297	0.8840	0.4673	*0.9736*
PSNR (dB)	∞	19.89	**40.25**	19.39	25.96	19.92	*36.73*
ERGAS	0	28.10	**3.51**	30.52	13.97	28.01	*4.19*

From the above results, among the different tested initialisation strategies, the approach based on the combination of VCA and FCLS stands out for its superior performance in terms of final fusion qualities. This superiority is observed for both tested values of the coefficient α, testifying the high robustness of this joint initialisation method. Furthermore, it should be noted that the other tested endmember extraction techniques, combined with FCLS, also produced acceptable performances: this indicates the robustness of the proposed fusion approach with respect to the initialisation points.

6.2.2. *Sensitivity analysis to the spectral variability penalisation/regularisation coefficient*

As mentioned above, the considered cost function for the hyperspectral image unmixing process, defined in (10), contains a regularisation/penalisation term, weighted by the coefficient α, that may constrain spectral variability. Therefore, a sensitivity analysis to this coefficient is an important task. Figure 5 below shows obtained fusion performances, using SAM and PSNR, of the designed fusion approach, on all tested synthetic datasets, with different values, between 0 and 10, of the coefficient α.

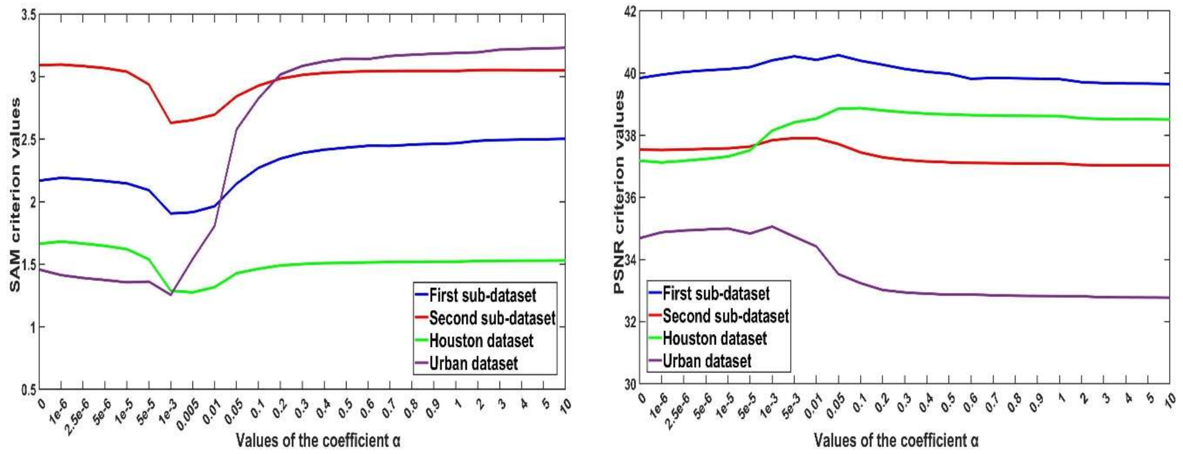

(a) (b)

Figure 5. Obtained (a) SAM (°) and (b) PSNR (dB) values, with different values of the coefficient α, for all considered synthetic datasets processed with the designed fusion approach.

From the above results, it appears that the different tested values of the coefficient α have some influence on fusion performances. A value of this coefficient in a typical range, between 5×10^{-5} and 2×10^{-1}, globally yields better performances, with the overall best performance for a value of α equal to 10^{-3}. Thus, this value is chosen for all carried out experiments.

6.2.3. *Results obtained with synthetic data*

In this subsection, results obtained by using the above-described synthetic datasets are provided in the following tables.

First, results obtained by using the two sub-datasets generated from the first considered synthetic dataset are presented in Tables III and IV.

Table III. Obtained performance values for the first sub-dataset generated from the first considered synthetic dataset (the bold values correspond to the best performances, and the italic underlined ones correspond to the second-best performances)

		Scenario	**Time (s)**	***SAM*** **(°)**	***SID***	***SSIM***	**PSNR (dB)**	**ERGAS**
	Ideal value			0	0	1	∞	0
Method	**Ext-CNMF-Var**		223.24	**1.62**	**0.10**	*0.9787*	*40.25*	**3.51**
	FSVA		42.97	2.36	**0.10**	**0.9820**	38.81	*3.73*
	DIFIV		>>	11.17	7.32	0.7390	20.78	22.05
	HMF-IPNMF		455.18	3.14	0.75	0.9125	34.67	9.51
	CNMF-Var		>>	*2.13*	0.44	0.9277	36.92	6.45
	Multi-JCNMF-Var		611.94	3.12	*0.15*	0.9767	**43.85**	5.19
	FuVar		279.18	3.87	1.35	0.8398	31.29	13.73
	SFIM		2.02	2.28	0.20	0.9698	38.81	7.15
	HySure	**(a)**	0.03	3.59	0.35	0.9513	38.26	6.64
		(b)	0.08	3.43	0.31	0.9563	39.01	6.04
	CNMF	**(a)**	1.58	7.70	1.63	0.8405	31.66	13.53
		(b)	2.68	6.67	1.85	0.8857	31.58	13.93

Table IV. Obtained performance values for the second sub-dataset generated from the first considered synthetic dataset (the bold values correspond to the best performances, and the italic underlined ones correspond to the second-best performances)

		Scenario	**Time (s)**	***SAM*** **(°)**	***SID***	***SSIM***	**PSNR (dB)**	**ERGAS**
	Ideal value			0	0	1	∞	0
Method	**Ext-CNMF-Var**		517,78	**2.14**	*0.16*	0.9653	**39.79**	*5.48*
	FSVA		75.10	8.21	1.01	0.9142	36.13	**4.86**
	DIFIV		>>	11.77	14.17	0.5953	16.64	25.94
	HMF-IPNMF		512.03	11.55	8.23	0.6731	31.71	15.83
	CNMF-Var		>>	5.12	0.53	0.9161	31.05	9.64
	Multi-JCNMF-Var		775.02	12.75	1.18	0.8910	29.84	17.27
	FuVar		896.49	10.13	0.67	0.9202	29.35	15.67
	SFIM		2.46	*4.67*	**0.12**	*0.9805*	35.69	7.36
	HySure	**(a)**	2.78	5.68	*0.16*	0.9757	36.91	7.50
		(b)	10.06	4.90	**0.12**	**0.9815**	*38.41*	6.09
	CNMF	**(a)**	1.45	8.59	0.55	0.9458	30.33	15.98
		(b)	2.35	12.01	1.26	0.8915	28.50	19.89

Globally, the above two tables show that the proposed Ext-CNMF-Var approach which addresses the spectral variability phenomenon yields the best performances, in terms of spectral and spatial reconstruction qualities, for the first tested synthetic dataset.

Indeed, for the first tested synthetic dataset, the proposed Ext-CNMF-Var approach most often reaches the best performance values in terms of spectral reconstruction quality, with a SAM value equal to 1.62° and a SID value equal to 0.10 obtained with the first tested sub-dataset, and a SAM value equal to 2.14° and a SID value equal to 0.16 obtained with the second tested sub-dataset. In a similar way, the proposed Ext-CNMF-Var algorithm achieves satisfactory performance values in terms of spatial reconstruction quality, with the second highest value for the SSIM criterion, equal to 0.9787, and also the second highest value for the PSNR criterion, equal to 40.25 dB, obtained with the first tested sub-dataset, and with a value for the SSIM criterion, equal to 0.9653, and the highest value for the PSNR criterion, equal to 39.79 dB, obtained with the second tested sub-dataset. Moreover, Tables III and IV show that the tested CNMF method, in the two considered scenarios, always achieves lower performances in terms of spectral and spatial reconstruction qualities than the designed Ext-CNMF-Var method, which considers the spectral variability phenomenon. The CNMF method reaches SAM values between 6.67° and 12.01°, and PSNR values between 28.50 dB and 31.66 dB.

Furthermore, Tables III and IV show that the tested literature methods which take into consideration the spectral variability phenomenon (i.e., FSVA, DIFIV, HMF-IPNMF, CNMF-Var, Multi-JCNMF-Var and FuVar) also yield fairly good performance in terms of spectral reconstruction for the first tested sub-dataset, with SAM values ranging from 2.13° to 11.17°, and lower performance for the second tested sub-dataset, with SAM values ranging from 5.12° to 12.75°. In terms of spatial reconstruction quality, the FSVA, DIFIV, HMF-IPNMF, CNMF-Var, Multi-JCNMF-Var and FuVar approaches provide PSNR values between 20.78 dB and 43.85 dB with the first tested sub-dataset, and values between 16.64 dB and 36.13 dB with the second tested sub-dataset. They provide SSIM values between 0.7390 and 0.9820 with the first tested sub-dataset, and values between 0.5953 and 0.9202 with the second tested sub-dataset.

As an illustration, Figure 6 shows, for the first sub-dataset generated from the first considered synthetic dataset, the true-color image composite of the reference hyperspectral image and sharpened hyperspectral images obtained with all tested methods. Figure 7 shows the normalized SAM criterion maps calculated between the reference image and the estimated sharpened data. The obtained SAM values are normalized, here between 0 and 1, by dividing the obtained results for each tested method by the maximum angle reached on the considered data, to improve the visualization of smallest errors and to ensure that the obtained results, with the different tested fusion methods, are compared at the same scale. Figure 8 illustrates the obtained PSNR values for each hyperspectral spectral band.

Reference
Ext-CNMF-Var
FSVA
DIFIV
HMF-IPNMF
CNMF-Var
Multi-JCNMF-Var
FuVar
SFIM
HySure (scenario: b)
CNMF (scenario: b)

Figure 6. True-color image composite for the first sub-dataset generated from the first considered synthetic dataset.

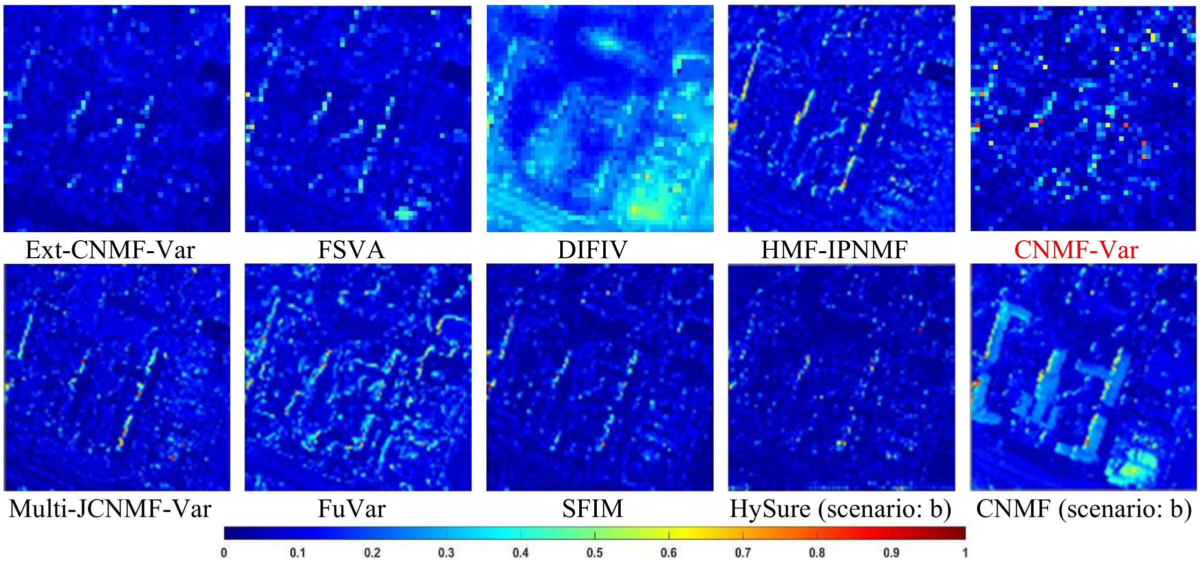

Figure 7. Normalized SAM values obtained between the reference image and the estimated sharpened data for the first sub-dataset generated from the first considered synthetic dataset.

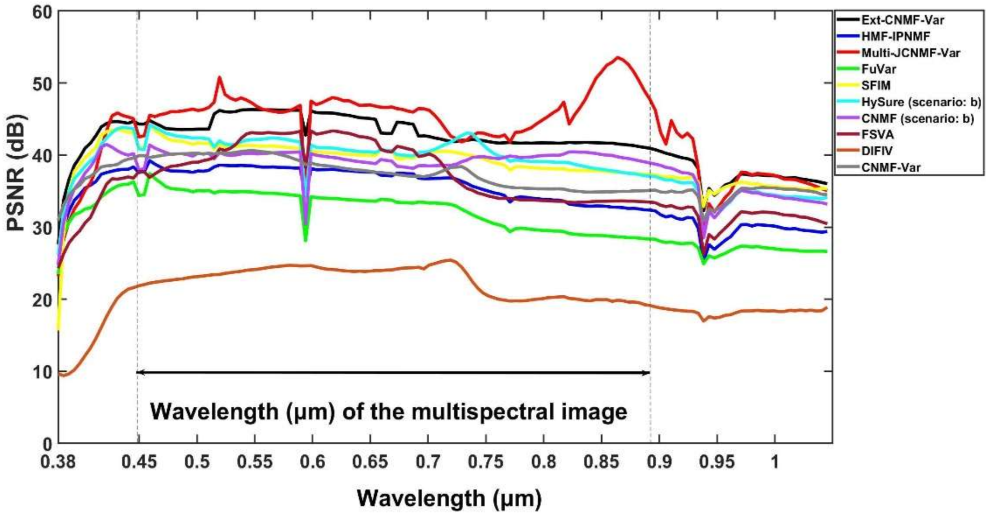

Figure 8. Obtained PSNR values (dB), for each hyperspectral spectral band, for the first sub-dataset generated from the first considered synthetic dataset.

In the following, the results obtained using the Houston data are reported in Table V.

Table V. Obtained performance values for the considered Houston dataset (the bold values correspond to the best performances, and the italic underlined ones correspond to the second-best performances)

Method	**Scenario**	**Time (s)**	***SAM*** **(°)**	***SID***	***SSIM***	**PSNR (dB)**	**ERGAS**
Ideal value			0	0	1	∞	0
Ext-CNMF-Var		874.92	*1.56*	*0.06*	**0.9900**	*37.52*	*1.88*
FSVA		1230.92	1.88	0.14	0.9767	36.79	2.31
DIFIV		>>	23.18	19.96	0.7021	18.13	16.77
HMF-IPNMF		530.12	3.73	1.06	0.7833	25.58	4.46
CNMF-Var		>>	3.31	1.99	0.7705	21.84	14.47
Multi-JCNMF-Var		337.69	2.20	0.24	0.9429	33.32	2.87
FuVar		700.03	2.69	0.19	0.9583	32.43	3.22
SFIM		2.61	**1.40**	**0.05**	*0.9880*	**37.67**	**1.81**
HySure	**(a)**	8.70	1.86	0.10	0.9743	35.38	2.30
	(b)	34.95	1.65	0.08	0.9773	36.06	2.12
CNMF	**(a)**	0.39	8.27	1.09	0.9151	27.39	6.63
	(b)	0.60	9.29	2.39	0.8815	23.40	9.40

For the Houston data (i.e., the second considered synthetic dataset), Table V yields the following results: the proposed Ext-CNMF-Var approach achieves the best SSIM criterion value, equal to 0.9900, and a SAM criterion value, equal to 1.56°, while the tested literature methods which address spectral variability give SAM values ranging from 1.88° to 23.18°, and from 1.40° to 9.29° for the tested methods that do not deal with the considered phenomenon (namely SFIM, HySure and CNMF). Furthermore, among the latter three methods, SFIM provides, in general, better performances, in terms of spectral and spatial reconstruction criteria. Moreover, SFIM is directly followed by the designed Ext-CNMF-Var approach for the criteria SAM, SID, PSNR and ERGAS.

Here also, as an illustration, Figures 9-11 show, for the considered synthetic Houston hyperspectral dataset, the visual results (the sharpened images, the normalized SAM values and the obtained PSNR values) obtained with the tested approaches.

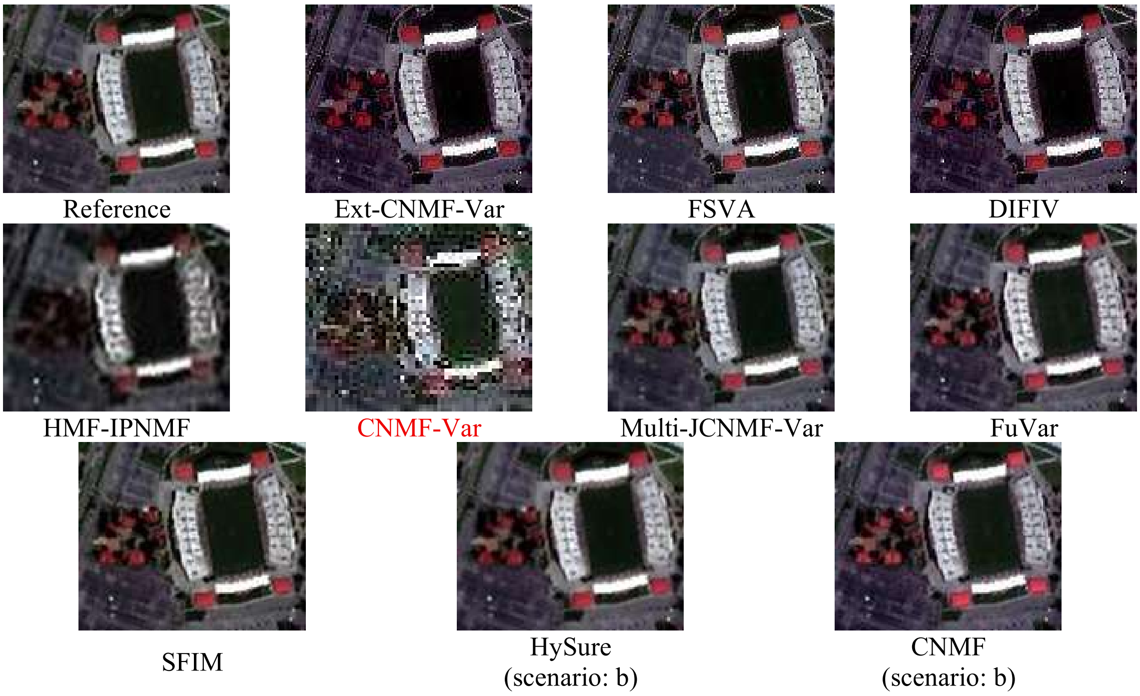
Reference
Ext-CNMF-Var
FSVA
DIFIV
HMF-IPNMF
CNMF-Var
Multi-JCNMF-Var
FuVar
SFIM
HySure (scenario: b)
CNMF (scenario: b)

Figure 9. True-color image composite for the data obtained from the second considered synthetic dataset (Houston data).

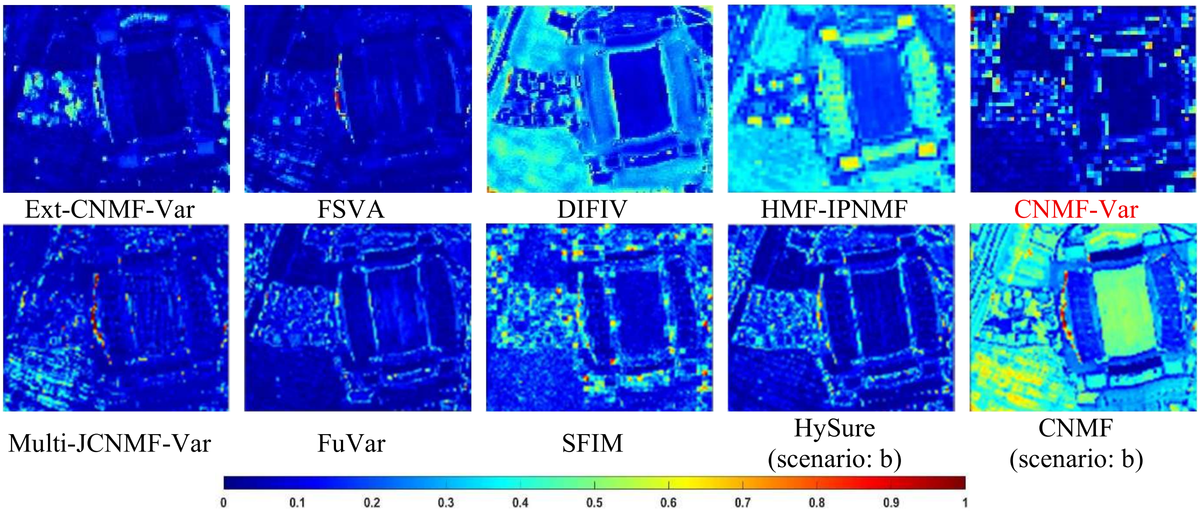
Ext-CNMF-Var
FSVA
DIFIV
HMF-IPNMF
CNMF-Var
Multi-JCNMF-Var
FuVar
SFIM
HySure (scenario: b)
CNMF (scenario: b)

Figure 10. Normalized SAM values obtained between the reference image and the estimated sharpened data for the second considered synthetic dataset (Houston data).

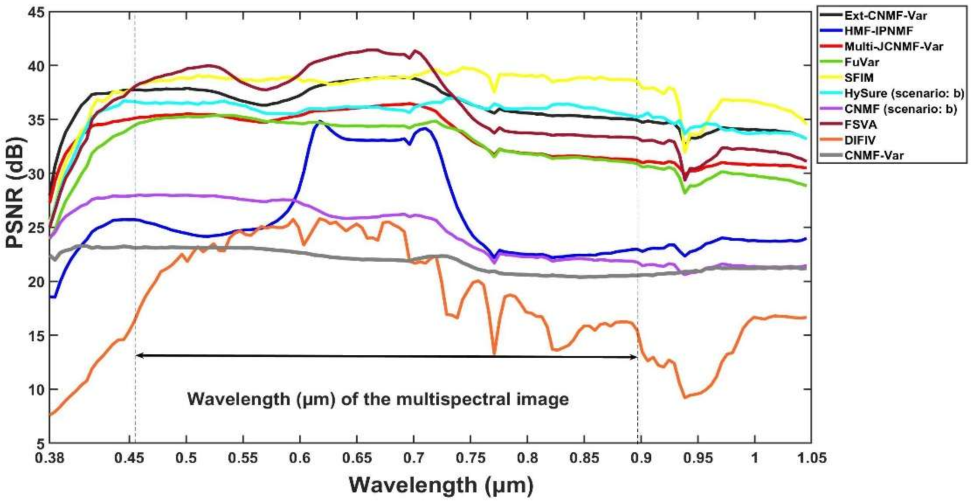

Figure 11. Obtained PSNR values (dB), for each hyperspectral spectral band, for the data obtained from the second considered synthetic dataset (Houston data).

Finally, the results obtained from the Urban data are summarized in Table VI.

Table VI. Obtained performance values for the considered Urban dataset (the bold values correspond to the best performances, and the italic underlined ones correspond to the second-best performances)

Method		Scenario	Time (s)	*SAM* (°)	*SID*	*SSIM*	PSNR (dB)	ERGAS
	Ideal value			0	0	1	∞	0
	Ext-CNMF-Var		1989.22	*1.15*	**0.03**	**0.9907**	**35.40**	**1.53**
	FSVA		2519.70	5.88	0.51	0.8805	25.93	7.60
	DIFIV		>>	9.36	6.48	0.7991	21.21	17.35
	HMF-IPNMF		600.18	3.13	0.24	*0.9572*	25.77	4.87
	CNMF-Var		>>	4.40	0.78	0.9249	*30.27*	8.38
	Multi-JCNMF-Var		570.52	**0.71**	*0.12*	0.9312	28.44	*3.53*
	FuVar		120.98	3.40	0.28	0.8531	24.49	5.27
	SFIM		12.08	2.13	0.22	0.8754	25.75	4.52
	HySure	**(a)**	4.19	2.03	0.22	0.8784	25.78	4.45
		(b)	6.17	2.14	0.22	0.8761	25.68	4.49
	CNMF	**(a)**	6.84	5.69	0.39	0.9193	23.08	6.14
		(b)	9.02	6.55	0.60	0.8858	21.62	7.39

Regarding the Urban data (i.e., the third considered synthetic dataset), Table VI also confirms that the sharpened data obtained using the proposed approach exhibit overall better spatial and spectral fidelities. In fact, the Ext-CNMF-Var method results in a SAM value equal to 1.15° and a SID value equal to 0.03. In terms of spatial reconstruction evaluation criteria, this method yields a SSIM value equal to 0.9907, a PSNR value equal to 35.40 dB, and an ERGAS value equal to 1.53. Besides, the tested literature methods (i.e., methods that take into account spectral variability as well as those that do not), provide, in terms of spectral reconstruction evaluation criteria, SAM values between 0.71° and 9.36°, and SID values between 0.12 and 6.48. Similarly, for all tested literature methods, the range of obtained SSIM values is 0.7991-0.9572. For the PSNR values, the range, for these tested literature methods, is 21.21-30.27 dB.

In the following, Figures 12-14 illustrate, for the considered synthetic Urban hyperspectral dataset, the visual results (the sharpened images, the normalized SAM values and the obtained PSNR values) achieved with the tested approaches.

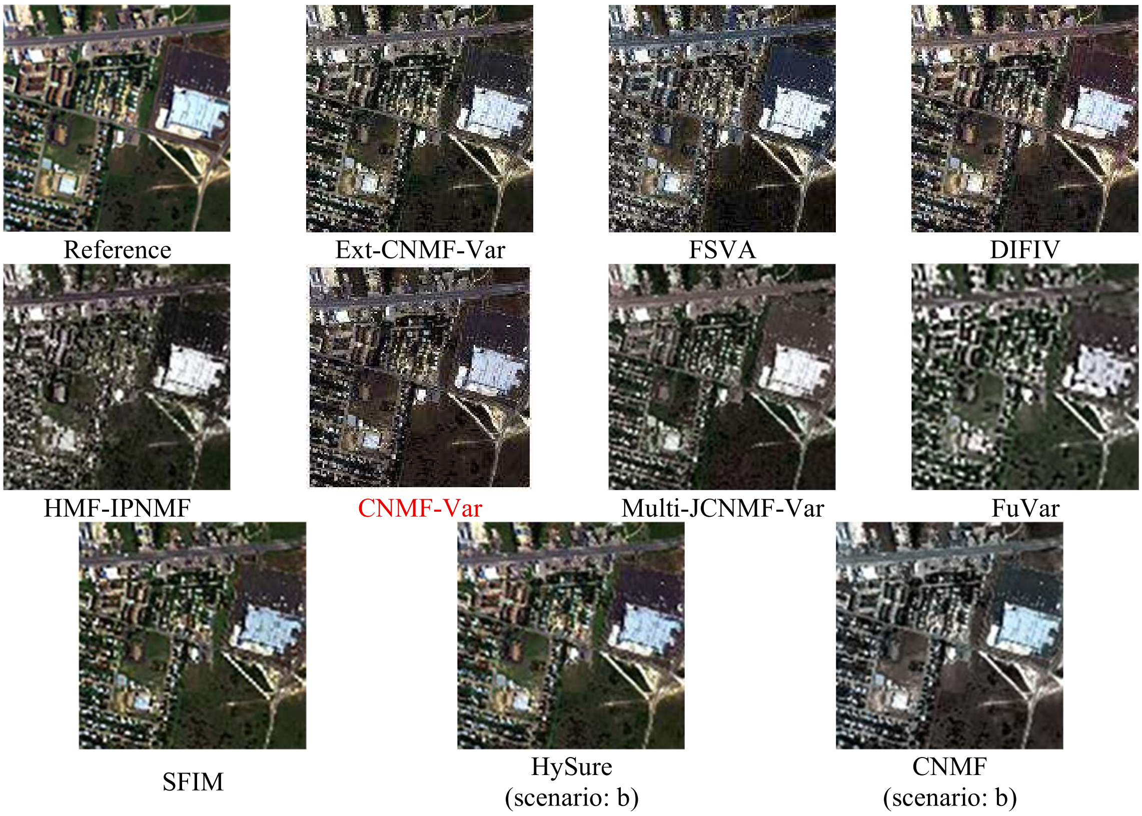
Reference
Ext-CNMF-Var
FSVA
DIFIV
HMF-IPNMF
CNMF-Var
Multi-JCNMF-Var
FuVar
SFIM
HySure
(scenario: b)
CNMF
(scenario: b)

Figure 12. True-color image composite for the data obtained from the third considered synthetic dataset (Urban data).

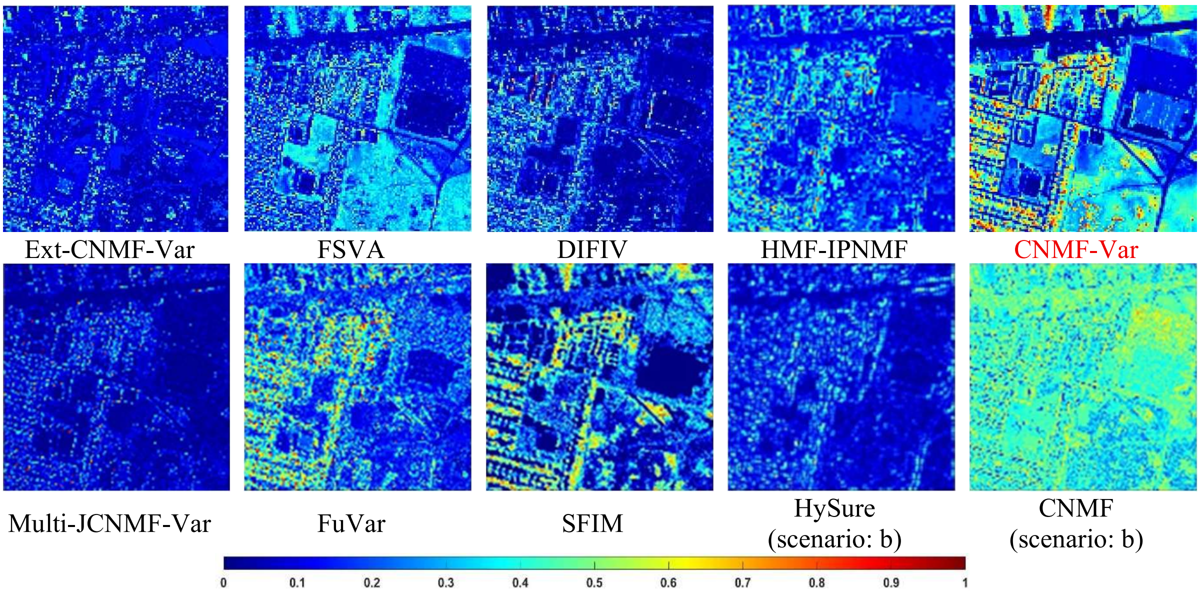

Ext-CNMF-Var FSVA DIFIV HMF-IPNMF CNMF-Var

Multi-JCNMF-Var FuVar SFIM HySure (scenario: b) CNMF (scenario: b)

Figure 13. Normalized SAM values obtained between the reference image and the estimated sharpened data for the third considered synthetic dataset (Urban data).

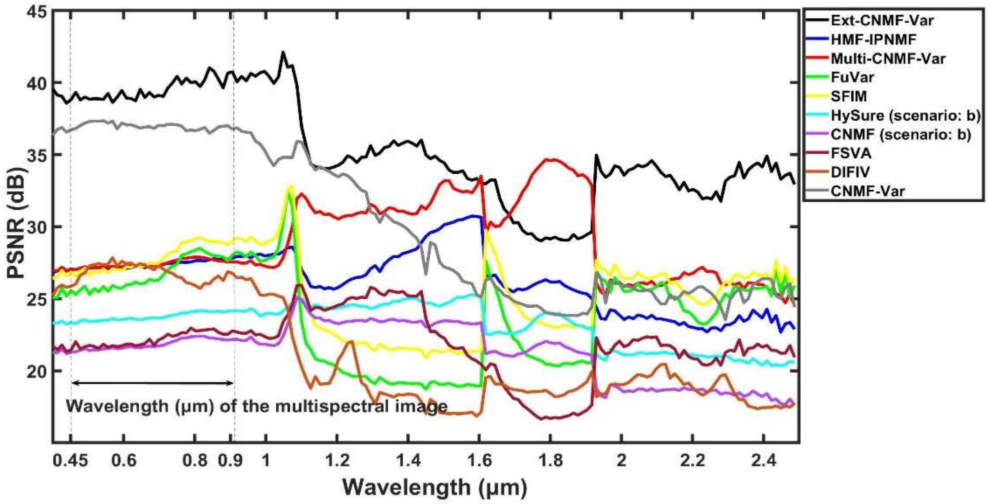

Figure 14. Obtained PSNR values (dB), for each hyperspectral spectral band, for the data obtained from the third considered synthetic dataset (Urban data).

Based on the results of these tests carried out on synthetic data, it can be concluded that, globally, the above tables show that the methods which address the spectral variability phenomenon (i.e., Ext-CNMF-Var, FSVA, DIFIV, HMF-IPNMF, CNMF-Var, Multi-JCNMF-Var and FuVar) yield the best performances, in terms of spectral and spatial reconstruction qualities, with improved overall performance for the designed Ext-CNMF-Var approach, which also has an acceptable execution time. Indeed, the comparative analysis with classical and DL-based methods, which consider or not spectral variability, demonstrated the robustness, interpretability and adaptability of the proposed unsupervised unmixing-based fusion approach, while its model-based construction and its independence from training data make it an interesting contribution to the hyperspectral and multispectral data fusion field. Furthermore, a particular point may be highlighted: only when the spectral bands of the considered multispectral image cover a larger part of the spectral bands of the hyperspectral image, the SFIM method also provides satisfactory fusion performances, but with an overall superiority for the designed approach. This global superiority confirms the robustness of the designed method, particularly when the spectral bands of the multispectral image cover a limited part of those of the hyperspectral image. These results confirm the relevance of the proposed approach, which offers better generalisation and more consistent performances when faced with a variety of data.

In terms of visual inspection, the above-provided figures (Figures 6-14), when considering synthetic data, confirm the good overall performance of the designed Ext-CNMF-Var algorithm. Indeed, the proposed method yields sharpened images with relatively lower spatial and spectral distortions in comparison with the other tested literature approaches, some of which generate many spatial and spectral distortions.

6.2.4. *Results obtained with real data*

The following table (Table VII) shows the performance values obtained by using the first real data described above. Note here that for these first real data, the assumed number of classes of endmembers is set to 7. The next figure (Figure 15) shows the low spatial resolution hyperspectral image and the estimated sharpened ones.

Table VII. Obtained performance values for the first considered real data (the bold values correspond to the best performances, and the italic underlined ones correspond to the second-best performances).

		Scenario	Time (s)	D_λ	D_s	mQNR
	Ideal value			0	0	1
Method	**Ext-CNMF-Var**		934.96	0.0164	**0.0393**	**0.9449**
	FSVA		1196.74	0.0284	0.3330	0.6481
	DIFIV		>>	0.0968	0.2900	0.6413
	HMF-IPNMF		411.23	0.1381	0.1161	0.7618
	CNMF-Var		>>	0.0126	0.1423	0.8469
	Multi-JCNMF-Var		471.80	*0.0084*	*0.0487*	*0.9433*
	FuVar		50.48	0.0719	0.0568	0.8753
	SFIM		4.29	**0.0038**	0.0642	0.9317
	HySure	**(a)**	1.22	0.0882	0.2130	0.7175
		(b)	15.51	0.0974	0.2258	0.6988
	CNMF	**(a)**	0.48	0.0353	0.1376	0.8319
		(b)	2.38	0.0475	0.2947	0.6718

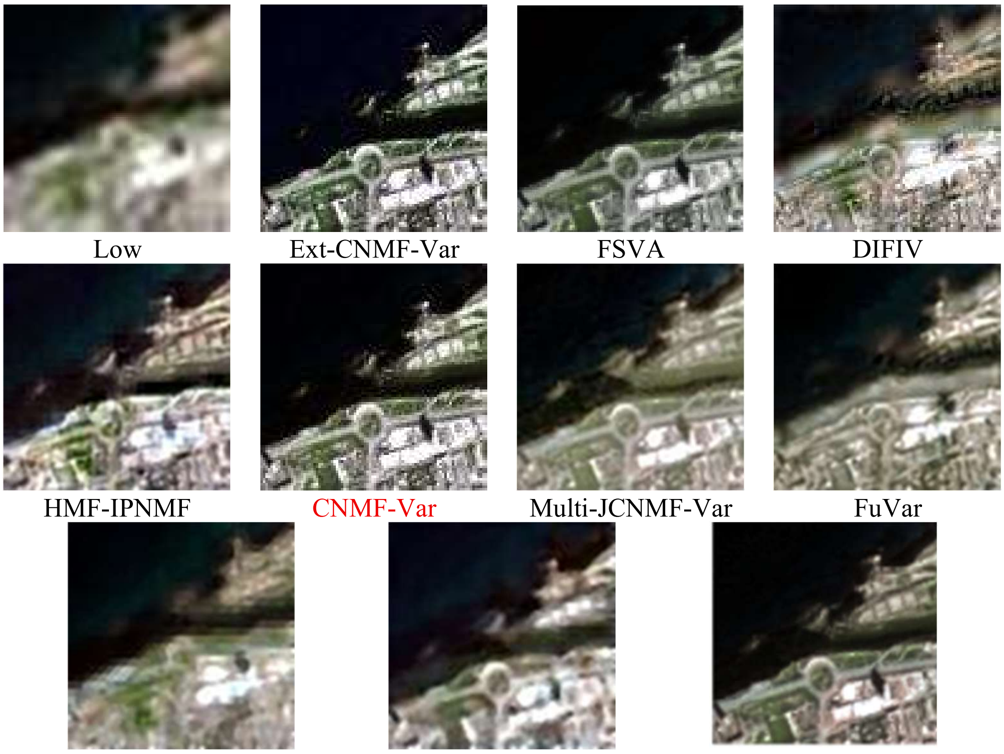
Low
Ext-CNMF-Var
FSVA
DIFIV
HMF-IPNMF
CNMF-Var
Multi-JCNMF-Var
FuVar
SFIM
HySure
(scenario: b)
CNMF
(scenario: b)

Figure 15. Color image composite for the first considered real data.

When considering the first real data, Table VII also confirms the overall good performances of the designed Ext-CNMF-Var method in comparison with the considered literature ones, in particular in terms of the spatial distortion index D_s and the mQNR.

In terms of visual inspection, as can be seen from Figure 15, the sharpened image obtained with the designed CNMF-based unmixing approach gives rather better visual results than the tested methods from the literature.

The following table (Table VIII) shows the performance values obtained by using the second tested real data described above.

Table VIII. Obtained performance values for the second considered real data (the bold values correspond to the best performances, and the italic underlined ones correspond to the second-best performances).

Method		Scenario	Time (s)	D_λ	D_s	mQNR
	Ideal value			0	0	1
	Ext-CNMF-Var		1783.17	**0.0158**	0.1764	**0.8106**
	FSVA		4139.43	0.0333	0.2701	0.7057
	DIFIV		>>	0.0839	0.1576	0.7717
	HMF-IPNMF		1021.35	0.2304	0.0894	0.7008
	CNMF-Var		>>	*0.0216*	0.2257	0.7574
	Multi-JCNMF-Var		516.09	0.1900	*0.0130*	0.7995
	FuVar		2617.37	0.1928	0.0663	0.7536
	SFIM		15.53	0.1904	**0.0045**	*0.8059*
	HySure	**(a)**	58.50	0.2547	0.0366	0.7180
		(b)	92.64	0.2487	0.0490	0.7146
	CNMF	**(a)**	26.21	0.2942	0.0330	0.6825
		(b)	29.09	0.3446	0.3322	0.4377

Regarding the second tested real dataset, Table VIII shows the good overall performance of the proposed Ext-CNMF-Var method compared to the other tested approaches from the literature. In particular, this method stands out for its low spectral distortion index (D_λ), with a value equal to 0.0158, as well as an mQNR criterion value equal to 0.8106, thus demonstrating its robustness.

The next figure (Figure 16) shows the low spatial resolution hyperspectral image and the estimated sharpened ones.

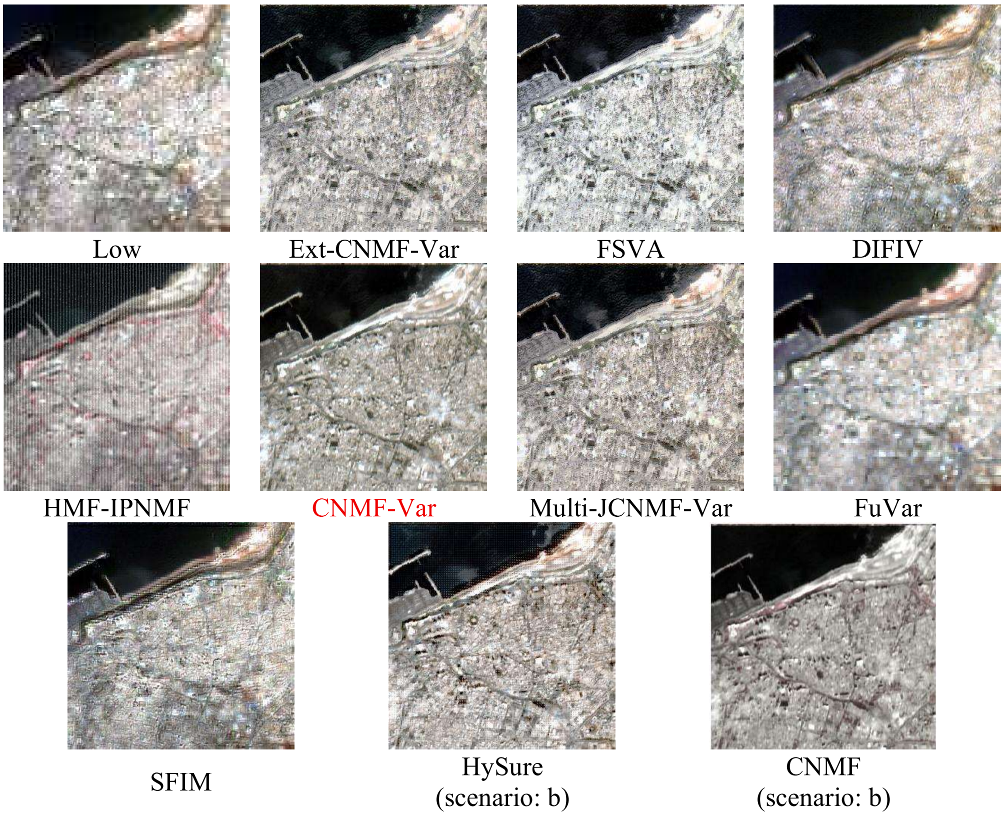
Low Ext-CNMF-Var FSVA DIFIV
HMF-IPNMF CNMF-Var Multi-JCNMF-Var FuVar
SFIM HySure (scenario: b) CNMF (scenario: b)

Figure 16. Color image composite for the second tested real data.

Finally, it should be noted here that the provided computational costs (for all the performed tests) are only indicative and are not used as a comparison criterion. These computational costs (where the symbol “>>” corresponds to an execution time exceeding one hour) are given so that readers may just have an idea about the execution time of each used method. Indeed, it is difficult to compare, using the computational costs, differently designed methods. Moreover, it is clear that fusion methods that consider the spectral variability phenomenon have a higher computational cost. This is mainly due to the structure of their algorithms, as well as the sizes of the considered variables in this type of algorithms, which are obviously larger than those of the considered variables in the fusion approaches that do not take into account the spectral variability phenomenon.

Overall, the proposed Ext-CNMF-Var fusion method tends to achieve better results thanks to its ability to explicitly model spectral variability when considering hyperspectral data. This characteristic significantly improves the extraction of spectra from hyperspectral data, taking into account the spectral variations present in the processed image. In addition, the adopted approach is based on a coupled unmixing process between hyperspectral and multispectral data. This process results in an alternating update of the variables derived from these two types of data. Thus, accurate extraction of spectra indirectly leads to more reliable estimation of abundance fraction maps derived from multispectral data. As a result, the obtained sharpened image benefits from a high-quality spectral reconstruction, preserving both spatial detail and the fidelity of spectral signatures.

In summary, and as expected and mentioned in the Motivations and Contributions section, obtained results, from all conducted experiments, confirm that the designed unsupervised model-based unmixing-based fusion approach, which deals with a wider class of spectral variability, globally outperforms tested non-unmixing-based and unmixing-based fusion methods that do not consider spectral variability or those which take into account a less broad class of this phenomenon. Moreover, it globally performs better than the tested unsupervised DL-based data-driven approach. It runs with a computation time that can be improved, in future works, using parallel processing or dimensionality reduction, with which it could also manage large data.

7. Conclusion

In this paper, an approach was proposed for fusing high spectral resolution hyperspectral images with high spatial resolution multispectral remote sensing images. This approach is based on an NMF technique that substantially extends the multiplicative CNMF algorithm to a specific structure of optimised matrices that deal with the phenomenon of spectral variability.

Once all the involved variables have been appropriately initialised, the proposed approach consists in alternately updating hyperspectral and multispectral variables in a coupled manner using an outer loop. First, one linearly unmixes the hyperspectral data, in a first inner loop, using a data mixing model that takes into account the spectral variability phenomenon modelled in a multiplicative form. The hyperspectral endmember spectra obtained in this first unmixing process are then down-sampled to the wavelength domains considered in the multispectral image and are used as an initialization of the spectra considered in the second unmixing process (in a second inner loop), that deals with the multispectral image. Following this second unmixing process, the obtained high spatial resolution abundance fractions are spatially down-sampled and are used as an initialisation (in the next iteration of the first inner loop) of the abundance fractions in the hyperspectral unmixing process. This entire process is repeated until the last iteration of the considered outer loop. Finally, the obtained high spectral and spatial resolution parts of information are recombined, according to the considered data mixing model, which takes into account the phenomenon of spectral variability, to obtain high spectral and spatial resolutions hyperspectral data.

The designed method was applied to synthetic and real data, and its performances were evaluated by using conventional criteria. Experimental results demonstrate that the introduced approach yields sharpened hyperspectral data with quite good spectral and spatial fidelities. Also, this approach globally performs better than the tested literature fusion methods.

An interesting extension of this work may consist in using, in the spectral unmixing process, a new data mixing model that handles both spectral variability and non-linearity phenomena, in order to address, in addition to variations in illumination and atmospheric conditions, the case of non-flat landscapes and/or lighting heterogeneity in the imaged area.

Acknowledgments: The authors would like to thank all the authors of the state-of-the-art fusion methods for making their source codes available for comparison.

References

Alparone, Luciano, Bruno Aiazzi, Stefano Baronti, Andrea Garzelli, Filippo Nencini, and Massimo Selva. 2008. "Multispectral and Panchromatic Data Fusion Assessment Without Reference." Photogrammetric Engineering & Remote Sensing 74 (2): 193–200. doi:10.14358/PERS.74.2.193.

Benhalouche, Fatima Zohra, Moussa Sofiane Karoui, Salah Eddine Brezini, Yannick Deville, and Yasmine Kheira Benkouider. 2022. "Hypersharpening Based on Extended Coupled Nonnegative Matrix Factorization Addressing Spectral Variability." In 2022 IEEE Mediterranean and Middle-East Geoscience and Remote Sensing Symposium (M2GARSS), 70–73. Istanbul, Turkey: IEEE. doi:10.1109/M2GARSS52314.2022.9840261.

Benhalouche, Fatima Zohra, Moussa Sofiane Karoui, and Yannick Deville. 2019. "An NMF-Based Approach for Hyperspectral Unmixing Using a New Multiplicative-Tuning Linear Mixing Model to Address Spectral Variability." In 2019 27th European Signal Processing Conference (EUSIPCO), 1–5. A Coruna, Spain: IEEE. doi:10.23919/EUSIPCO.2019.8902707.

Benhalouche, Fatima Zohra, Moussa Sofiane Karoui, Yannick Deville, and Abdelaziz Ouamri. 2017. "Hyperspectral and Multispectral Data Fusion Based on Linear-Quadratic Nonnegative Matrix Factorization." Journal of Applied Remote Sensing 11 (2): 025008. doi:10.1117/1.JRS.11.025008.

Bioucas-Dias, José M., Antonio Plaza, Nicolas Dobigeon, Mario Parente, Qian Du, Paul Gader, and Jocelyn Chanussot. 2012. "Hyperspectral Unmixing Overview: Geometrical, Statistical, and Sparse Regression-Based Approaches." IEEE Journal of Selected Topics in Applied Earth Observations and Remote Sensing 5 (2): 354–379. doi:10.1109/JSTARS.2012.2194696.

Borsoi, Ricardo A., Clemence Prevost, Konstantin Usevich, David Brie, Jose C. M. Bermudez, and Cedric Richard. 2021. "Coupled Tensor Decomposition for Hyperspectral and Multispectral Image Fusion with Inter-Image Variability." IEEE Journal of Selected Topics in Signal Processing 15 (3): 702–717. doi:10.1109/JSTSP.2021.3054338.

Borsoi, Ricardo Augusto, Tales Imbiriba, and Jose Carlos Moreira Bermudez. 2020. "Super-Resolution for Hyperspectral and Multispectral Image Fusion Accounting for Seasonal Spectral Variability." IEEE Transactions on Image Processing 29: 116–127. doi:10.1109/TIP.2019.2928895.

Borsoi, Ricardo Augusto, Tales Imbiriba, José Carlos Moreira Bermudez, Cédric Richard, Jocelyn Chanussot, Lucas Drumetz, Jean-Yves Tourneret, Alina Zare, and Christian Jutten. 2021. "Spectral Variability in Hyperspectral Data Unmixing: A Comprehensive Review." IEEE Geoscience and Remote Sensing Magazine 9 (4): 223–270. doi:10.1109/MGRS.2021.3071158.

Boyd, Stephen. 2010. "Distributed Optimization and Statistical Learning via the Alternating Direction Method of Multipliers." Foundations and Trends® in Machine Learning 3 (1): 1–122. doi:10.1561/2200000016.

Brezini, Salah Eddine, Yannick Deville, Moussa Sofiane Karoui, Fatima Zohra Benhalouche, and Abdelaziz Ouamri. 2021. "A Penalization-Based NMF Approach for Hyperspectral Unmixing Addressing Spectral Variability with an Additively-Tuned Mixing Model." In 2021 IEEE International Geoscience and Remote Sensing Symposium IGARSS, 3841–3844. Brussels, Belgium: IEEE. doi:10.1109/IGARSS47720.2021.9553366.

Brezini, Salah Eddine, Moussa Sofiane Karoui, Fatima Zohra Benhalouche, Yannick Deville, and Abdelaziz Ouamri. 2022. "Hypersharpening by an NMF-Unmixing-Based Method Addressing Spectral Variability." IEEE Geoscience and Remote Sensing Letters 19: 1–5. doi:10.1109/LGRS.2021.3072405.

Camacho, Ariolfo, Edwin Vargas, and Henry Arguello. 2022. "Hyperspectral and Multispectral Image Fusion Addressing Spectral Variability by an Augmented Linear Mixing Model." International Journal of Remote Sensing 43 (5): 1577–1608. doi:10.1080/01431161.2022.2041762.

Chen, C-H, 2012. Twenty-Five Years of Pansharpening: A Critical Review and New Developments. 2012. In Signal and Image Processing for Remote Sensing. doi:10.1201/b11656-31.

Chang, Chein-I, Chao-Cheng Wu, Chien-Shun Lo, and Mann-Li Chang. 2010. "Real-Time Simplex Growing Algorithms for Hyperspectral Endmember Extraction." IEEE Transactions on Geoscience and Remote Sensing 48 (4): 1834–1850. doi:10.1109/TGRS.2009.2034979.

Chen, Zhao, Hanye Pu, Bin Wang, and Geng-Ming Jiang. 2014. "Fusion of Hyperspectral and Multispectral Images: A Novel Framework Based on Generalization of Pan-Sharpening Methods." IEEE Geoscience and Remote Sensing Letters 11 (8): 1418–1422. doi:10.1109/LGRS.2013.2294476.

Cichocki, Andrzej, Rafal Zdunek, Anh Huy Phan, and Shun-ichi Amari. 2009. Nonnegative Matrix and Tensor Factorizations: Applications to Exploratory Multi-Way Data Analysis and Blind Source Separation. John Wiley and Sons.

Debes, Christian, Andreas Merentitis, Roel Heremans, Jurgen Hahn, Nikolaos Frangiadakis, Tim Van Kasteren, Wenzhi Liao, et al. 2014. "Hyperspectral and LiDAR Data Fusion: Outcome of the 2013 GRSS Data Fusion Contest." IEEE Journal of Selected Topics in Applied Earth Observations and Remote Sensing 7 (6): 2405–2418. doi:10.1109/JSTARS.2014.2305441.

Deville, Yannick. 2016. "Blind Source Separation and Blind Mixture Identification Methods." In Wiley Encyclopedia of Electrical and Electronics Engineering, by John G. Webster, 1–33. Hoboken, NJ, USA: John Wiley & Sons, Inc. doi:10.1002/047134608X.W8300.

Dian, Renwei, Shutao Li, Anjing Guo, and Leyuan Fang. 2018. “Deep Hyperspectral Image Sharpening.” IEEE Transactions on Neural Networks and Learning Systems 29 (11): 5345–5355. doi:10.1109/TNNLS.2018.2798162.

Dian, Renwei, Shutao Li, Bin Sun, and Anjing Guo. 2021. “Recent Advances and New Guidelines on Hyperspectral and Multispectral Image Fusion.” Information Fusion 69 (May): 40–51. doi:10.1016/j.inffus.2020.11.001.

Drumetz, Lucas, Miguel-Angel Veganzones, Simon Henrot, Ronald Phlypo, Jocelyn Chanussot, and Christian Jutten. 2016. “Blind Hyperspectral Unmixing Using an Extended Linear Mixing Model to Address Spectral Variability.” IEEE Transactions on Image Processing 25 (8): 3890–3905. doi:10.1109/TIP.2016.2579259.

Eismann, M.T., and R.C. Hardie. 2005. “Hyperspectral Resolution Enhancement Using High-Resolution Multispectral Imagery with Arbitrary Response Functions.” IEEE Transactions on Geoscience and Remote Sensing 43 (3): 455–465. doi:10.1109/TGRS.2004.837324.

Gu, Jiafeng, Bin Yang, and Bin Wang. 2022. “Nonlinear Unmixing for Hyperspectral Images via Kernel-Transformed Bilinear Mixing Models.” IEEE Transactions on Geoscience and Remote Sensing 60: 1–13. doi:10.1109/TGRS.2021.3135571.

Halimi, Abderrahim, Yoann Altmann, Nicolas Dobigeon, and Jean-Yves Tourneret. 2011. “Nonlinear Unmixing of Hyperspectral Images Using a Generalized Bilinear Model.” IEEE Transactions on Geoscience and Remote Sensing 49 (11): 4153–4162. doi:10.1109/TGRS.2010.2098414.

Han, Zhu, Jin Yang, Lianru Gao, Zhiqiang Zeng, Bing Zhang, and Jocelyn Chanussot. 2025. “Subpixel Spectral Variability Network for Hyperspectral Image Classification.” IEEE Transactions on Geoscience and Remote Sensing 63: 1–14. doi:10.1109/TGRS.2025.3535749.

Heinz, D.C., and Chein-I Chang. 2001. “Fully Constrained Least Squares Linear Spectral Mixture Analysis Method for Material Quantification in Hyperspectral Imagery.” IEEE Transactions on Geoscience and Remote Sensing 39 (3): 529–545. doi:10.1109/36.911111.

Heylen, Rob, Mario Parente, and Paul Gader. 2014. “A Review of Nonlinear Hyperspectral Unmixing Methods.” IEEE Journal of Selected Topics in Applied Earth Observations and Remote Sensing 7 (6): 1844–1868. doi:10.1109/JSTARS.2014.2320576.

Heylen, Rob, and Paul Scheunders. 2016. “A Multilinear Mixing Model for Nonlinear Spectral Unmixing.” IEEE Transactions on Geoscience and Remote Sensing 54 (1): 240–251. doi:10.1109/TGRS.2015.2453915.

Hong, Danfeng, Naoto Yokoya, Jocelyn Chanussot, and Xiao Xiang Zhu. 2019. “An Augmented Linear Mixing Model to Address Spectral Variability for Hyperspectral Unmixing.” IEEE Transactions on Image Processing 28 (4): 1923–1938. doi:10.1109/TIP.2018.2878958.

Hu, Jin-Fan, Ting-Zhu Huang, Liang-Jian Deng, Tai-Xiang Jiang, Gemine Vivone, and Jocelyn Chanussot. 2022. “Hyperspectral Image Super-Resolution via Deep Spatiospectral Attention Convolutional Neural Networks.” IEEE Transactions on Neural Networks and Learning Systems 33 (12): 7251–7265. doi:10.1109/TNNLS.2021.3084682.

Huang, Bo, Song, Huihui, Cui, Hengbin, Peng, Jigen, and Xu, Zongben. 2014. “Spatial and Spectral Image Fusion Using Sparse Matrix Factorization," in IEEE Transactions on Geoscience and Remote Sensing 52 3: 1693–1704. doi: 10.1109/TGRS.2013.2253612.

Imbiriba, Tales, Ricardo Augusto Borsoi, and Jose Carlos Moreira Bermudez. 2018. “Generalized Linear Mixing Model Accounting for Endmember Variability.” In 2018 IEEE International Conference on Acoustics, Speech and Signal Processing (ICASSP), 1862–1866. Calgary, AB: IEEE. doi:10.1109/ICASSP.2018.8462214.

Karoui, Moussa Sofiane, Fatima Zohra Benhalouche, Salah Eddine Brezini, Yannick Deville, and Yasmine Kheira Benkouider. 2021. “Hypersharpening by a Multiplicative Joint-Criterion NMF Method Addressing Spectral Variability.” In 2021 IEEE International Geoscience and Remote Sensing Symposium IGARSS, 4472–4475. Brussels, Belgium: IEEE. doi:10.1109/IGARSS47720.2021.9553972.

Karoui, Moussa Sofiane, Fatima Zohra Benhalouche, and Yannick Deville. 2022. “Hyperspectral Unmixing with a Modified Augmented Linear Mixing Model Addressing Spectral Variability.” In Virtual Symposium. In 2022 IEEE Mediterranean and Middle-East Geoscience and Remote Sensing Symposium (M2GARSS), 70–73. Istanbul, Turkey: IEEE. doi: 10.1109/m2garss52314.2022.9839710.

Karoui, Moussa Sofiane, Yannick Deville, Fatima Zohra Benhalouche, and Issam Boukerch. 2017. “Hypersharpening by Joint-Criterion Nonnegative Matrix Factorization.” IEEE Transactions on Geoscience and Remote Sensing 55 (3): 1660 - 1670. doi: 10.1109/TGRS.2016.2628889.

Khader, Abdolraheem, Liang Xiao, and Jingxiang Yang. 2022. “A Model-Guided Deep Convolutional Sparse Coding Network for Hyperspectral and Multispectral Image Fusion.” International Journal of Remote Sensing 43 (6): 2268–2295. doi:10.1080/01431161.2021.1995073.

Li, Jiaxin, Ke Zheng, Jing Yao, Lianru Gao, and Danfeng Hong. 2022. “Deep Unsupervised Blind Hyperspectral and Multispectral Data Fusion.” IEEE Geoscience and Remote Sensing Letters 19: 1–5. doi:10.1109/LGRS.2022.3151779.

Lin, Chia-Hsiang, Fei Ma, Chong-Yung Chi, and Chih-Hsiang Hsieh. 2018. “A Convex Optimization-Based Coupled Nonnegative Matrix Factorization Algorithm for Hyperspectral and Multispectral Data Fusion.” IEEE Transactions on Geoscience and Remote Sensing 56 (3): 1652–1667. doi:10.1109/TGRS.2017.2766080.

Liu, J. G. 2000. “Smoothing Filter-Based Intensity Modulation: A Spectral Preserve Image Fusion Technique for Improving Spatial Details.” International Journal of Remote Sensing 21 (18): 3461–3472. doi:10.1080/014311600750037499.

Liu, Wenjie, Yongnian Zeng, Songnian Li, and Wei Huang. 2020. “Spectral Unmixing Based Spatiotemporal Downscaling Fusion Approach.” International Journal of Applied Earth Observation and Geoinformation 88 (June): 102054. doi:10.1016/j.jag.2020.102054.

Loncan, Laetitia, Luis B. De Almeida, Jose M. Bioucas-Dias, Xavier Briottet, Jocelyn Chanussot, Nicolas Dobigeon, Sophie Fabre, et al. 2015. “Hyperspectral Pansharpening: A Review.” IEEE Geoscience and Remote Sensing Magazine 3 (3): 27–46. doi:10.1109/MGRS.2015.2440094.

Lu, Xiaochen, Tong Li, Junping Zhang, and Fengde Jia. 2022. “A Novel Unmixing-Based Hypersharpening Method via Convolutional Neural Network.” IEEE Transactions on Geoscience and Remote Sensing 60: 1–14. doi:10.1109/TGRS.2021.3063105.

Lu, Xiaochen, Junping Zhang, Xiangzhen Yu, Wenming Tang, Tong Li, and Ye Zhang. 2019. “Hyper-Sharpening Based on Spectral Modulation.” IEEE Journal of Selected Topics in Applied Earth Observations and Remote Sensing 12 (5): 1534–1548. doi:10.1109/JSTARS.2019.2908984.

Luo, Wenfei, Lianru Gao, Antonio Plaza, Andrea Marinoni, Bin Yang, Liang Zhong, Paolo Gamba, and Bing Zhang. 2016. “A New Algorithm for Bilinear Spectral Unmixing of Hyperspectral Images Using Particle Swarm Optimization.” IEEE Journal of Selected Topics in Applied Earth Observations and Remote Sensing 9 (12): 5776–5790. doi:10.1109/JSTARS.2016.2602882.

Meganem, Ines, Philippe Deliot, Xavier Briottet, Yannick Deville, and Shahram Hosseini. 2014. “Linear–Quadratic Mixing Model for Reflectances in Urban Environments.” IEEE Transactions on Geoscience and Remote Sensing 52 (1): 544–558. doi:10.1109/TGRS.2013.2242475.

Nascimento, J.M.P., and J.M.B. Dias. 2005. “Vertex Component Analysis: A Fast Algorithm to Unmix Hyperspectral Data.” IEEE Transactions on Geoscience and Remote Sensing 43 (4): 898–910. doi:10.1109/TGRS.2005.844293.

Nascimento, José M. P., and José M. Bioucas-Dias. 2009. “Nonlinear Mixture Model for Hyperspectral Unmixing.” In SPIE 7477, Image and Signal Processing for Remote Sensing, XV:74770I. Berlin, Germany. doi:10.1117/12.830492.

Palsson, Frosti, Johannes R. Sveinsson, and Magnus O. Ulfarsson. 2017. “Multispectral and Hyperspectral Image Fusion Using a 3-D-Convolutional Neural Network.” IEEE Geoscience and Remote Sensing Letters 14 (5): 639–643. doi:10.1109/LGRS.2017.2668299.

Petersen, Kaare Brandt, and Michael Syskind Pedersen. 2012. “[Http://Matrixcookbook.Com].” Technical University of Denmark, November, 72.

Priya K., and Rajkumar K K. 2021. “Multiplicative Iterative Nonlinear Constrained Coupled Non-Negative Matrix Factorization (MINC-CNMF) for Hyperspectral and Multispectral Image Fusion.” International Journal of Advanced Computer Science and Applications 12 (6). doi:10.14569/IJACSA.2021.0120660.

Priya K., and Rajkumar K K. 2022. “Hyperspectral and Multispectral Image Fusion Using Fully Constrained Nonlinear Coupled Nonnegative Matrix Factorization.” ICTACT Journal on Image and Video Processing 12 (3): 2644–2649. doi:10.21917/ijivp.2022.0375.

Restaino, Rocco, Gemine Vivone, Paolo Addesso, Daniele Picone, and Jocelyn Chanussot. 2020. “Resolution Enhancement of Hyperspectral Data Exploiting Real Multi-Platform Data.” In Recent Advances in Image Restoration with Applications to Real World Problems, edited by Chiman Kwan. Rijeka: IntechOpen. doi:10.5772/intechopen.92795.

Revel, Charlotte, Yannick Deville, Véronique Achard, Xavier Briottet, and Christiane Weber. 2018. “Inertia-Constrained Pixel-by-Pixel Nonnegative Matrix Factorisation: A Hyperspectral Unmixing Method Dealing with Intra-Class Variability.” Remote Sensing 10 (11): 1706. doi:10.3390/rs10111706.

Selva, Massimo, Bruno Aiazzi, Francesco Butera, Leandro Chiarantini, and Stefano Baronti. 2015. “Hyper-Sharpening: A First Approach on SIM-GA Data.” IEEE Journal of Selected Topics in Applied Earth Observations and Remote Sensing 8 (6): 3008–3024. doi:10.1109/JSTARS.2015.2440092.

Simoes, Miguel, Jose Bioucas-Dias, Luis B. Almeida, and Jocelyn Chanussot. 2015. “A Convex Formulation for Hyperspectral Image Superresolution via Subspace-Based Regularization.” IEEE Transactions on Geoscience and Remote Sensing 53 (6): 3373–3388. doi:10.1109/TGRS.2014.2375320.

Sun, Shasha, Wenxing Bao, Kewen Qu, Wei Feng, Xuan Ma, and Xiaowu Zhang. 2024. “Hyperspectral-Multispectral Image Fusion Using Subspace Decomposition and Elastic Net Regularization.” International Journal of Remote Sensing 45 (12): 3962–3991. doi:10.1080/01431161.2024.2357840.

Thouvenin, Pierre-Antoine, Nicolas Dobigeon, and Jean-Yves Tourneret. 2016. “Hyperspectral Unmixing with Spectral Variability Using a Perturbed Linear Mixing Model.” IEEE Transactions on Signal Processing 64 (2): 525–538. doi:10.1109/TSP.2015.2486746.

Tsagkatakis, Grigorios, Anastasia Aidini, Konstantina Fotiadou, Michalis Giannopoulos, Anastasia Pentari, and Panagiotis Tsakalides. 2019. “Survey of Deep-Learning Approaches for Remote Sensing Observation Enhancement.” Sensors 19 (18): 3929. doi:10.3390/s19183929.

Vali, Ava, Sara Comai, and Matteo Matteucci. 2020. “Deep Learning for Land Use and Land Cover Classification Based on Hyperspectral and Multispectral Earth Observation Data: A Review.” Remote Sensing 12 (15): 2495. doi:10.3390/rs12152495.

Vivone, Gemine. 2023. “Multispectral and Hyperspectral Image Fusion in Remote Sensing: A Survey.” Information Fusion 89 (January): 405–417. doi:10.1016/j.inffus.2022.08.032.

Vivone, Gemine, Luciano Alparone, Jocelyn Chanussot, Mauro Dalla Mura, Andrea Garzelli, Giorgio A. Licciardi, Rocco Restaino, and Lucien Wald. 2015. “A Critical Comparison Among Pansharpening Algorithms.” IEEE Transactions on Geoscience and Remote Sensing 53 (5): 2565–2586. doi:10.1109/TGRS.2014.2361734.

Vivone, Gemine, Mauro Dalla Mura, Andrea Garzelli, Rocco Restaino, Giuseppe Scarpa, Magnus O. Ulfarsson, Luciano Alparone, and Jocelyn Chanussot. 2021. “A New Benchmark Based on Recent Advances in Multispectral Pansharpening: Revisiting Pansharpening with Classical and Emerging Pansharpening Methods.” IEEE Geoscience and Remote Sensing Magazine 9 (1): 53–81. doi:10.1109/MGRS.2020.3019315.

Vivone, Gemine, Liang-Jian Deng, Shangqi Deng, Danfeng Hong, Menghui Jiang, Chenyu Li, Wei Li, et al. 2025. “Deep Learning in Remote Sensing Image Fusion: Methods, Protocols, Data, and Future Perspectives.” IEEE Geoscience and Remote Sensing Magazine 13 (1): 269–310. doi:10.1109/MGRS.2024.3495516.

Wald, Lucien. 1997. “Fusion of Satellite Images of Different Spatial Resolutions: Assessing the Quality of Resulting Images,” 9.

Wald, Lucien. 2000. “Quality of High-Resolution Synthesised Images: Is There a Simple Criterion?” In Fusion of Earth Data: Merging Point Measurements, Raster Maps and Remotely Sensed Images, 3:99–103. Sophia Antipolis, France.

Wang, T., H. Zhang, and H. Lin. 2017. “Using Coupled Nonnegative Matrix Factorization (CNMF) Un-Mixing for High Spectral and Spatial Resolution Data Fusion to Estimate urban Impervious Surface and Urban Ecological Environment.” The International Archives of the Photogrammetry, Remote Sensing and Spatial Information Sciences XLII-2/W7 (September): 919–923. doi:10.5194/isprs-archives-XLII-2-W7-919-2017.

Wang, Xiuheng, Ricardo Augusto Borsoi, Cédric Richard, and Jie Chen. 2023. “Deep Hyperspectral and Multispectral Image Fusion with Inter-Image Variability.” IEEE Transactions on Geoscience and Remote Sensing 61: 1–15. doi:10.1109/TGRS.2023.3273118.

Wang, Zhengjue, Bo Chen, Hao Zhang, and Hongwei Liu. 2022. “Unsupervised Hyperspectral and Multispectral Images Fusion Based on Nonlinear Variational Probabilistic Generative Model.” IEEE Transactions on Neural Networks and Learning Systems 33 (2): 721–735. doi:10.1109/TNNLS.2020.3028772.

Winter, Michael E. 1999. “N-FINDR: An Algorithm for Fast Autonomous Spectral End-Member Determination in Hyperspectral Data.” In SPIE’s International Symposium on Optical Science, Engineering, and Instrumentation, edited by Michael R. Descour and Sylvia S. Shen, 3753:266–275. Denver, CO, United States. doi:10.1117/12.366289.

Xu, S., and M. Ehlers. 2022. “Critical Reflection on Quantitative Assessment of Image Fusion Quality.” The International Archives of the Photogrammetry, Remote Sensing and Spatial Information Sciences XLIII-B3-2022 (May): 551–557. doi:10.5194/isprs-archives-XLIII-B3-2022-551-2022.

Yang, Bin, Bin Wang, and Zongmin Wu. 2018. “Nonlinear Hyperspectral Unmixing Based on Geometric Characteristics of Bilinear Mixture Models.” IEEE Transactions on Geoscience and Remote Sensing 56 (2): 694–714. doi:10.1109/TGRS.2017.2753847.

Yokoya, Naoto, Claas Grohnfeldt, and Jocelyn Chanussot. 2017. “Hyperspectral and Multispectral Data Fusion: A Comparative Review of the Recent Literature.” IEEE Geoscience and Remote Sensing Magazine 5 (2): 29–56. doi:10.1109/MGRS.2016.2637824.

Yokoya, Naoto, Takehisa Yairi, and Akira Iwasaki. 2012. “Coupled Nonnegative Matrix Factorization Unmixing for Hyperspectral and Multispectral Data Fusion.” IEEE Transactions on Geoscience and Remote Sensing 50 (2): 528–537. doi:10.1109/TGRS.2011.2161320.

Zare, Alina, and K.C. Ho. 2014. “Endmember Variability in Hyperspectral Analysis: Addressing Spectral Variability During Spectral Unmixing.” IEEE Signal Processing Magazine 31 (1): 95–104. doi:10.1109/MSP.2013.2279177.

Zheng, Haoren, Zulong Li, Chenyu Sun, Hanqiu Zhang, Hongyi Liu, and Zhihui Wei. 2024. “Blind Unmixing Using Dispersion Model-Based Autoencoder to Address Spectral Variability.” IEEE Transactions on Geoscience and Remote Sensing 62: 1–14. doi:10.1109/TGRS.2024.3399003.

Zhou Wang, and A.C. Bovik. 2002. “A Universal Image Quality Index.” IEEE Signal Processing Letters 9 (3): 81–84. doi:10.1109/97.995823.

Zhu, Feiyun, Ying Wang, Bin Fan, Shiming Xiang, Geofeng Meng, and Chunhong Pan. 2014. “Spectral Unmixing via Data-Guided Sparsity.” IEEE Transactions on Image Processing 23 (12): 5412–5427. doi:10.1109/TIP.2014.2363423.